Core and Energy Estimations for SWGO Using a Template-based Shower Reconstruction Method

Master's Thesis in Physics

Presented by
Franziska Leitl
25.06.2021

Erlangen Centre for Astroparticle Physics
Friedrich-Alexander-Universität Erlangen-Nürnberg

Supervisor: Prof. Dr. Christopher van Eldik

Abstract

The Southern Wide-field Gamma-ray Observatory (SWGO) is a future ground-based particle detector array that will be used to detect cosmic gamma rays and other cosmic rays with energies in-between a few tens of GeV to hundreds of TeV [14]. Its particle detection method is based on the water Cherenkov detection technique which measures the Cherenkov light in the detectors once an Extensive Air Shower (EAS) hits the array. One task of the future array will be the analysis of cosmic gamma rays and their origins. With the help of a template-based reconstruction method, gamma-ray induced EASs can be reconstructed.

In this thesis, this template-based method is used to obtain core and energy estimations for reconstructing gamma-ray induced particle showers for SWGO. For this purpose, three different array layouts are tested.

In the beginning, a test layout that uses double-layered water Cherenkov detector (WCD) units was designed. Estimations regarding the core and energy reconstruction of vertical showers and showers with a zenith angle of 45° were made with the test array. At first, only the upper cells (UCs) of the WCD units were used. Then, the process was repeated using the whole detector unit. It was shown that using the lower cells (LCs) of the tanks in addition to the UCs, both in case of reconstructing vertical showers and showers with a zenith angle of 45°, does not change the performance of the reconstruction significantly since no saturation threshold has been implemented for the WCD units yet.

Next, the performance of reconstructing showers with the reference configuration of SWGO was assessed by reconstructing showers with a zenith angle of up to 45° that were thrown on the inner array of the reference configuration. The results for core and energy estimations were found to be promising for showers with a primary energy between a few tens of GeV and 100 TeV. The performance at higher energies could not be assessed because of limited statistics.

Lastly, different array layouts were designed with the super configuration of SWGO that were used as an extension of the reference configuration. Because of limited statistics for the super configuration, only preliminary estimations were made for the core and energy reconstruction.

Contents

1 Introduction **6**

2 Preparations **8**
2.1 Cosmic Rays 8
2.2 Production Processes of Gamma Rays 10
2.2.1 Synchrotron Radiation 11
2.2.2 Bremsstrahlung 12
2.2.3 Inverse Compton Scattering 12
2.2.4 Neutral Pion Decay 13
2.3 Fundamentals of Cosmic Gamma Ray Detection 14
2.3.1 Extensive Air Showers 15
2.3.2 Cherenkov Light 16
2.3.3 Ground-based Gamma-ray Detection Methods 17

3 The Southern Wide-field Gamma-ray Observatory (SWGO) **19**

4 Shower Reconstruction Method **23**
4.1 Likelihood Method 23
4.2 Template Generation 24
4.3 Template Smoothing 26
4.4 Fitting Procedure 26
4.5 Reconstruction of an Example Event 29

5 Test Array Layout **33**
5.1 Test Array Layout and Shower Simulations 33
5.2 Core and Energy Estimation 34
5.2.1 Upper and Lower Cells 35
5.2.2 Shower Reconstruction with θ_0 and θ_{45} 39
5.3 Bin Optimisation 42
5.3.1 Core Bin Optimisation 43
5.3.2 Energy Bin Optimisation 45
5.3.3 X_{max} Bin Optimisation 47

6 SWGO Reference Configuration **50**
6.1 Reference Configuration 50
6.2 Performance 52
6.2.1 Core Estimation 52

6.2.2 Energy Estimation 52

7 SWGO Super Configuration **55**
7.1 Layout of the Super Configuration 55
7.2 First Performance Tests 58
7.2.1 Core Estimation 58
7.2.2 Energy Estimation 59

8 Summary and Outlook **62**

Appendix **64**

References **71**

Acronyms **73**

Chapter 1

Introduction

The discovery of cosmic rays can be traced back to the Austrian physicist Victor Hess. In 1912, he started a series of experiments in which he used a hot air balloon to measure the radiation on Earth at different altitudes up to a height of around 5 km. At that time, the influence of the cosmic radiation was still unknown and the origin of the measurable radiation was mainly explained due to the natural radiation of the Earth. It was expected that the radiation measured in the balloon experiment would decrease steadily with an increasing altitude. As a matter of fact, this behaviour was seen in Hess' investigations up to an altitude of around 1000 m, but he noticed a renewed increase in radiation at higher altitudes. To explain his new discoveries, he made the assumption that there must be a previously undiscovered, additional radiation component on Earth which hits the surface of the Earth from above [12]. This radiation was first named Höhenstrahlung. Over the following years, many more experiments regarding the Höhenstrahlung were conducted. Since then, its origins are traced back to galactic and extragalactic sources which is why it is now more commonly referred to as cosmic radiation.

Today, the study of cosmic rays and their origins is an important part of modern astrophysics. In general, cosmic radiation consists of both charged and uncharged particles. However, to study its source, it is better to analyse the uncharged portion of the radiation as it does not get deflected on its way to Earth. Cosmic gamma rays are particularly suitable for this purpose which is why, nowadays, there exist a lot of different measurement techniques for these particles which are used by many different research groups all over the world.
One way of investigating cosmic gamma rays, in particular, is through ground-based detector techniques. The Southern Wide-field Gamma-ray Observatory (SWGO) is a future ground-based gamma ray particle detector array that will be build to investigate gamma rays and other cosmic rays with energies between a few tens of GeV to hundreds of TeV [14].

The goal of this thesis is to obtain first core and energy estimations for the reconstruction of gamma-ray induced air showers for SWGO with the help of a template-based reconstruction method. At first, a small introduction to cosmic rays is given and the main production processes of cosmic gamma rays and the fundamentals that are used for their

detection are explained. After an overview over SWGO, its goals and its planned design, the template-based method that is used for the shower reconstruction is described in detail. The results of the core and energy estimations for SWGO that could be attained through this work are given in chapters 5-7. In general, core and energy estimations were obtained for three different layouts, a test layout, the reference configuration of SWGO and the SWGO super configuration which will act as a generalisation of the reference design. In the end, all results are summarised and a short outlook regarding the future work concerning core and energy estimations for SWGO is given.

Chapter 2

Preparations

In this chapter, at first, a brief introduction to cosmic rays is given. Then, physical basics for the work done in this thesis are discussed. Since the focus of this thesis lies on the reconstruction of showers that were induced by gamma rays, these basics include the most important processes that lead to the production of gamma radiation in the first place and the basics of detecting cosmic gamma radiation. With regard to the detection method used by SWGO, the ground-based detection of gamma radiation is discussed in particular.

2.1 Cosmic Rays

Cosmic rays are high-energy particles that originate from either galactic or extragalactic sources. They can be charged as well as uncharged particles. A general distinction is made between primary and secondary cosmic rays. Primary cosmic rays are the cosmic rays that enter the atmosphere of the Earth. After a certain amount of time, these primary particles interact with the nuclei of the atmosphere and create new particles. These new particles are defined as secondary cosmic rays.

The spectrum of the cosmic rays, that has been measured so far, spans over several decades of energies. As can be seen in figure 2.1, previous experiments have been able to measure particles with energies of up to an order of magnitude of $10^{20}\,\mathrm{eV}$. Within this spectrum, which is also called the all-particle spectrum, a few specific features can be found at certain energy ranges. These features are defined as the knee, the second knee and the ankle of the spectrum [21]. To make those features more visible, the y-axis of the all-particle spectrum in figure 2.1 is amplified by a factor of $E^{2.6}$.

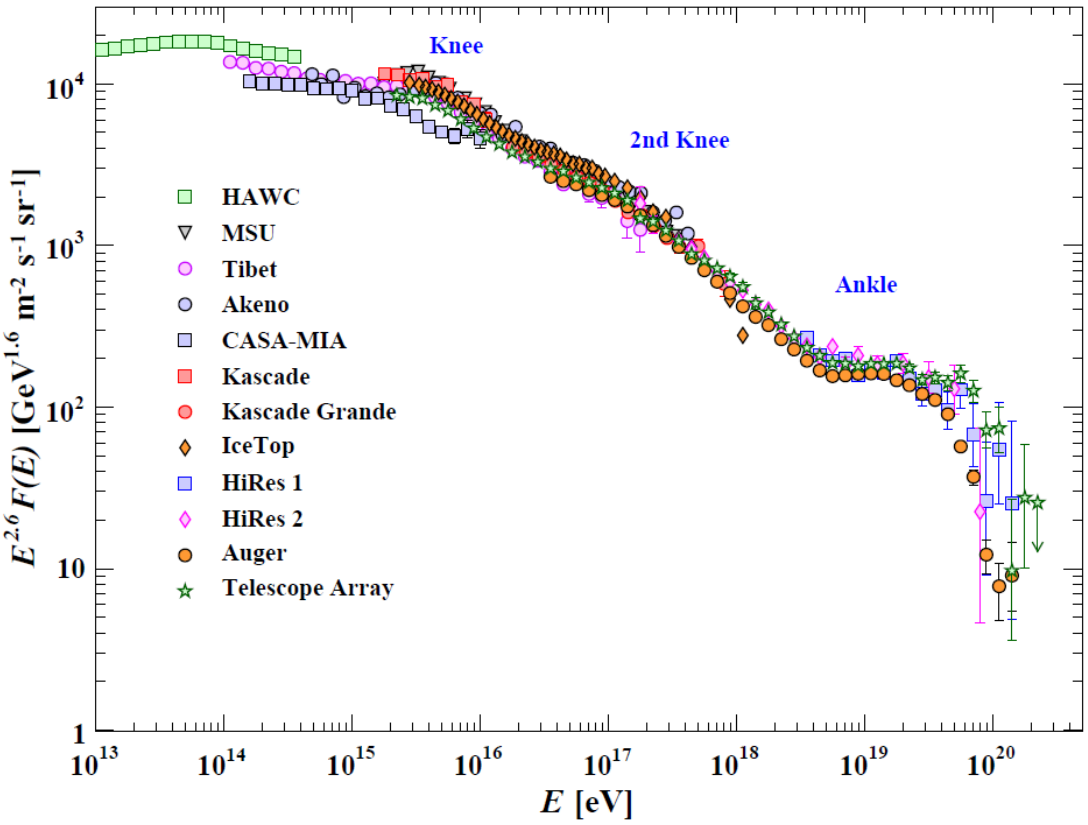

Figure 2.1: Cosmic ray spectrum that has been measured by a multitude of experiments. The y-axis is amplified by a factor of $E^{2.6}$ to make the knee, second knee and ankle more visible (figure taken from [21]).

The all-particle spectrum can be divided into multiple parts. The first part of the spectrum goes up to energies in the order of 10^{15} eV. After that, between 10^{15} eV and 10^{16} eV, the second section begins with the knee. Here, a first steepening occurs in the slope of the spectrum. After the second knee, which is located at around 10^{17} eV, the inclination increases a second time. Assuming a high percentage of the cosmic rays that can be measured on Earth originate from galactic sources, one finds a first explanation for the decrease of the flux after the first knee. Particles can only be held, and therefore measured, within our galaxy if their centrifugal force is smaller or equal to the Lorentz force of the Milky Way. By equating both functions one finds

$$\frac{mv^2}{r} = Z \cdot e \cdot v \cdot B \tag{2.1}$$

and

$$p = e \cdot r \cdot B \tag{2.2}$$

for particles with a singular charge. Here, r describes the radius after which the particles leave the Milky way, B the magnetic field of the Milky Way and p the impulse of a particle. Using equation 2.2, one can calculate the impulse of particles that do not fulfil this condition and, therefore, escape from the Milky Way. This value coincides with an energy in the order of 10^{15} eV at which the first knee is located [10].

Supernova remnants, which are considered to be particle accelerators of cosmic rays, also contribute to the decline in the particle flux after the first knee because they cannot accelerate particles to energies higher than ones in the order of 10^{15} eV [21].
The decrease after the second knee in the all-particle spectrum could be caused by the iron nuclei that start leaving the galaxy around that energy [10].
At energies in the order of 10^{19} eV the last feature in the spectrum, the ankle, is visible. It starts the last section of the all-particle spectrum which consists of particles that are assumed to result from extragalactic sources [10]. After that, a cut-off can be found which is defined as Greisen-Zatsepin-Kuzmin (GZK) cut-off. More information regarding this cut-off and measurements of particles with energies in the order of 10^{20} eV can be found in [8] and [10].

A lot of the sources of cosmic rays are still unknown. Finding those sources is further complicated by the fact that a large portion of the cosmic radiation, specifically the charged component, cannot be traced back to its point of origin. On their way from their original source to the Earth, charged cosmic rays do not travel in a straight path. Instead, they are deflected by interstellar magnetic fields such as the magnetic field of the sun.
This problem can be circumvented by analysing uncharged cosmic particles, like gamma rays. They are unaffected by the interstellar magnetic fields which means their trajectory can be reconstructed and their origin can be reproduced.

2.2 Production Processes of Gamma Rays

In this section, some of the main production processes of gamma rays are discussed. This includes the production of gamma rays through synchrotron radiation, Bremsstrahlung, the gamma-ray production through inverse Compton scattering and neutral pion decay [18]. Figure 2.2 shows an example for the energy ranges in which different production processes occur.

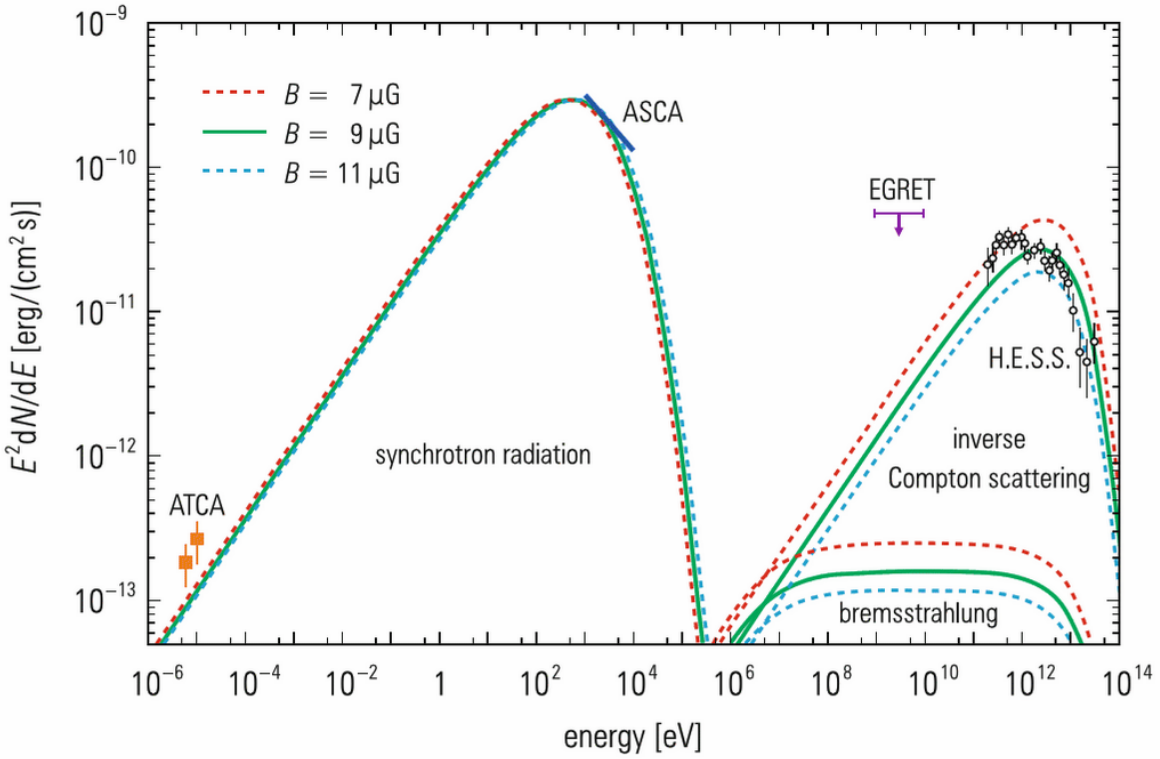

Figure 2.2: Spectrum of gamma rays with the contribution of different emission processes and measurements of ATCA (Australia Telescope Compact Array), ASCA (Advanced Satellite for Cosmology and Astrophysics), EGRET (Energetic Gamma Ray Experiment Telescope) and H.E.S.S. (High Energy Stereoscopic System) (figure taken from [10]).

2.2.1 Synchrotron Radiation

If a charged particle is travelling through a magnetic field along the magnetic field lines, it propagates in a spiral motion and is accelerated. Through this motion, the charged particle experiences an energy loss in the form of synchrotron radiation where photons are emitted from the propagating particle [18]. This process is depicted in figure 2.3. In figure 2.2 one can see that the contribution of synchrotron radiation to the gamma-ray spectrum lasts up to energies in the order of 10^5 eV.

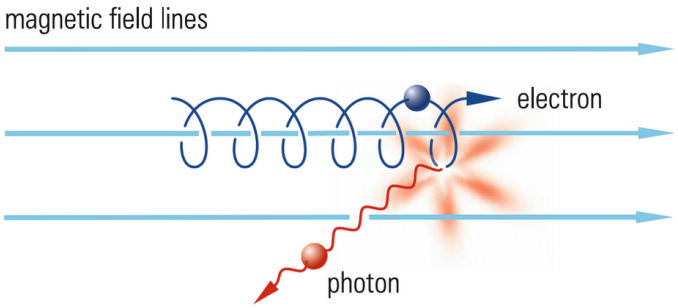

Figure 2.3: Production of synchrotron radiation by the deflection of an electron in a magnetic field (figure taken from [10]).

2.2.2 Bremsstrahlung

If charged particles interact with matter and are deflected in the Coulomb-field of an atom or a nucleus, radiation is emitted (see figure 2.4). This radiation is called Bremsstrahlung. For an electron, the energy that is lost after a certain distance can be calculated using

$$\frac{\mathrm{d}E_e}{\mathrm{d}x} = \frac{4nZ^2\alpha^3(\hbar c)^2 E_e}{m_e^2 c^4} \cdot \ln \frac{a(E)}{Z^{1/3}} \tag{2.3}$$

where E_e is the kinetic energy of the electron, c is the speed of light, n the density and Z the charge of the atom which interacts with the electron and $\alpha = e^2/(4\pi\epsilon_0\hbar c)$ is the fine-structure constant. The parameter a takes the distance between the electron and the atom into account which is necessary to still make deflection possible. The radiation length

$$X_0 = \left(\frac{4nZ^2\alpha^3(\hbar c)^2}{m_e^2 c^4} \cdot \ln \frac{a(E)}{Z^{1/3}} \right)^{-1} \tag{2.4}$$

describes the length after which the energy of an high-energy electron is at $1/e$. The energy range in which the Bremsstrahlung contributes to the energy spectrum of the gamma rays stretches from around 10^6 eV to around 10^{13} eV as can be seen in figure 2.2.

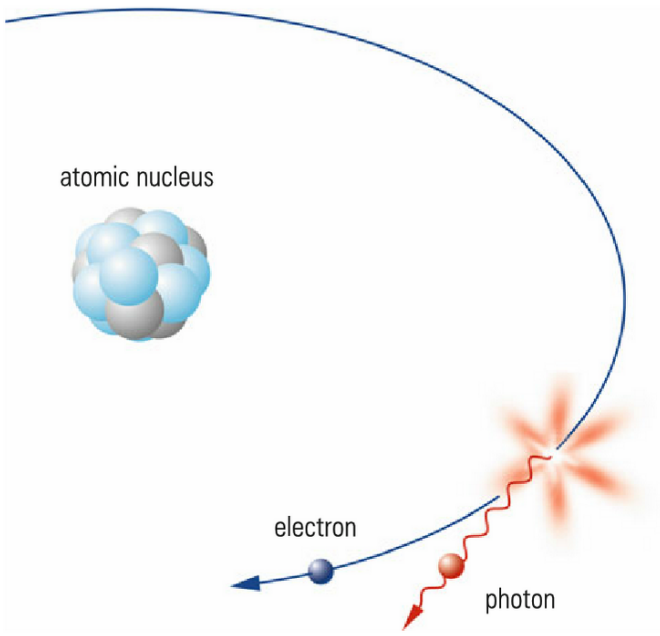

Figure 2.4: Production of Bremsstrahlung by the deflection of an electron in the Coulomb-field of a nucleus (figure taken from [10]).

2.2.3 Inverse Compton Scattering

Another way to produce gamma rays is via inverse Compton scattering where a low energy photon scatters with a high energy electron. The electron transfers a part of its energy to the photon resulting in a lower energy electron and high energy photon (see figure 2.5). For the production of cosmic gamma rays, the low energy photons often

stem from, for example, the cosmic microwave background or starlight [10]. Inverse Compton scattering contributes to the gamma ray spectrum in an energy range between 10^6 eV and 10^{14} eV (see figure 2.2).

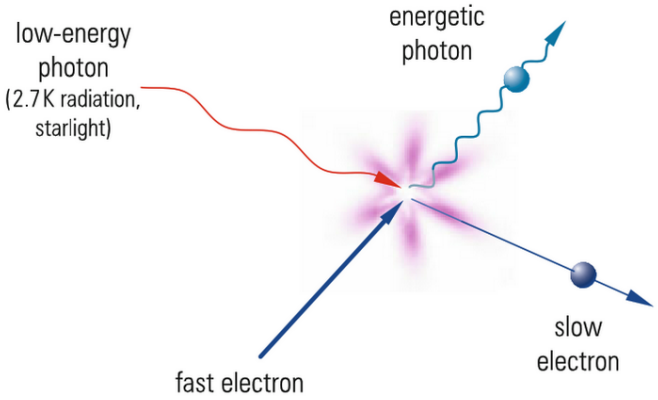

Figure 2.5: Inverse Compton scattering of a low energy photon with a high energy electron (figure taken from [10]).

2.2.4 Neutral Pion Decay

The production of gamma rays is also possible through the eventual decay of a π^0. When a proton collides with another proton or a nucleus of the interstellar medium, charged pions π^+ and π^- and neutral pions π^0 are created with equal probability. The neutral pion will then decay into two photons with a decay time of $\tau = 8.4 \cdot 10^{-17}$ s [18]. A possible decay which is described by

$$p + \text{nucleus} \rightarrow p' + \text{nucleus}' + \pi^0 + \pi^- + \pi^+$$

and

$$\pi^0 \rightarrow \gamma + \gamma$$

can be seen in figure 2.6. Whether the pion decays in motion or at rest will influence the energy of the resulting gamma rays. In motion, the two gamma rays will have a different energy from each other that is defined by the energy of the pion, the emission direction and the direction in which the pion has been travelling originally. If it decays at rest, both photons will have the same energy which amounts to half of the rest mass of the pion $m_{\pi^0} = 135\,\text{MeV}$ [10].

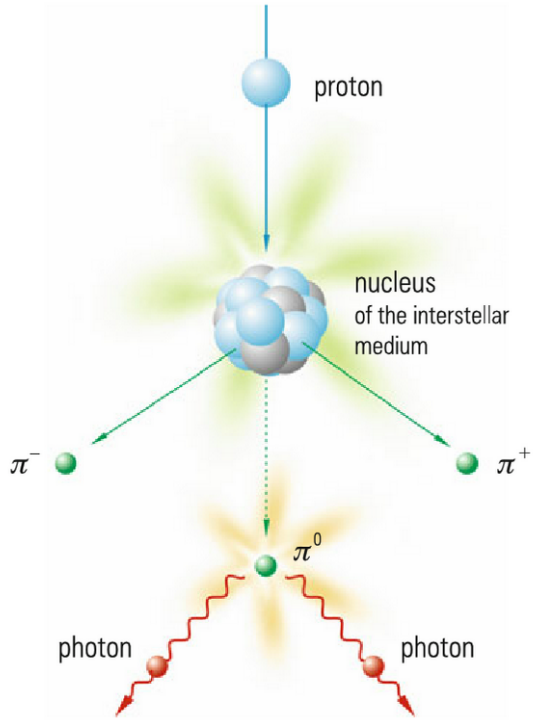

Figure 2.6: Production of gamma rays through the decay of π^0 (figure taken from [10]).

2.3 Fundamentals of Cosmic Gamma Ray Detection

The method which is used to detect cosmic gamma rays travelling towards Earth depends on the primary energy of the photon. The incoming flux of cosmic gamma rays is a lot higher for photons with lower energies than it is for photons with higher energies. This means that the required detection area of cosmic gamma rays depends on their energy. Since a smaller detection area is sufficient for lower energy cosmic gamma rays, they are often measured via space telescopes. One example for such would be the Large Area Telescope (Fermi-LAT)[5].
However, for the measurement of very high-energy gamma rays, a very large area is required to ensure sufficient statistics. This is difficult to implement for space telescopes. Instead, ground-based detection techniques are applied. Rather than measuring the primary gamma rays, they use an indirect detection where the secondary cosmic rays, that are created after the interaction between the primary rays and the nuclei in the atmosphere, are investigated.

In the following, the creation processes and characteristics of secondary particle showers, specifically the ones caused by gamma rays, and the production of Cherenkov light are explained. Finally, an overview over ground-based detection methods that are used to investigate cosmic gamma rays is given.

2.3.1 Extensive Air Showers

The initial interaction between a primary particle and the nuclei in the atmosphere will create a shower of secondary cosmic rays which is called an Extensive Air Shower (EAS). The composition of an EAS and its form will depend on the primary particle.
While charged primary cosmic rays will lead to a hadronic shower (see figure 2.7b) with typically wider lateral distributions and hadronic and electromagnetic shower components, uncharged primary rays will lead to electromagnetic showers (see figure 2.7a). Because the focus of this thesis is on the reconstruction of gamma-ray induced, electromagnetic air showers, the hadronic EASs will not be discussed here. Instead, an insight on electromagnetic showers is given. For a closer look at hadronic showers see, for example, [10].

The formation of an electromagnetic shower is triggered by the primary gamma ray reacting with the nuclei in the atmosphere. The course of such a shower (see figure 2.7a) will be described now in a simplified way following [19]. The shower can be divided into different stages n. After each stage, the number of particles in the shower increases until the maximum number of particles is reached. Here, the increase of the number of particles is assumed to either be caused by electron-positron pair production or via Bremsstrahlung. If a gamma ray triggers the next reaction, then the electron-positron pair production occurs as follows

$$\gamma \rightarrow e^+e^-. \tag{2.5}$$

The resulting electrons and positrons can in turn produce new photons with the help of Bremsstrahlung which has already been explained in section 2.2.2. In case of the e^+e^--production, the reaction can only occur as long as the previous gamma ray has an energy of at least the rest mass of an electron and a positron. The energy that is transferred to both resulting particles is equal.
The number of particles at each level n of the shower can be described by

$$N = 2^n = \mathrm{e}^{x/X_0} \tag{2.6}$$

and the shower depth is described by

$$x = nX_0 \ln 2 \tag{2.7}$$

where X_0 describes the radiation depth of the particle in a specific medium. After a certain amount of decays $N_{\max}$ the critical energy E_c, after which the energy loss of the particles via ionisation will be greater than the energy loss through Bremsstrahlung, will be reached. This causes the number of shower particles to decrease again for each of the following stages until the entire energy is absorbed and the shower vanishes. The maximum shower depth $X_{\max}$ can be calculated using

$$X_{\max} = X_0 \frac{\ln E_0/E_\mathrm{c}}{\ln 2} \tag{2.8}$$

where E_0 describes the energy of the primary gamma ray. The size of the electromagnetic shower is hereby assumed to be proportional to the primary energy E_0.

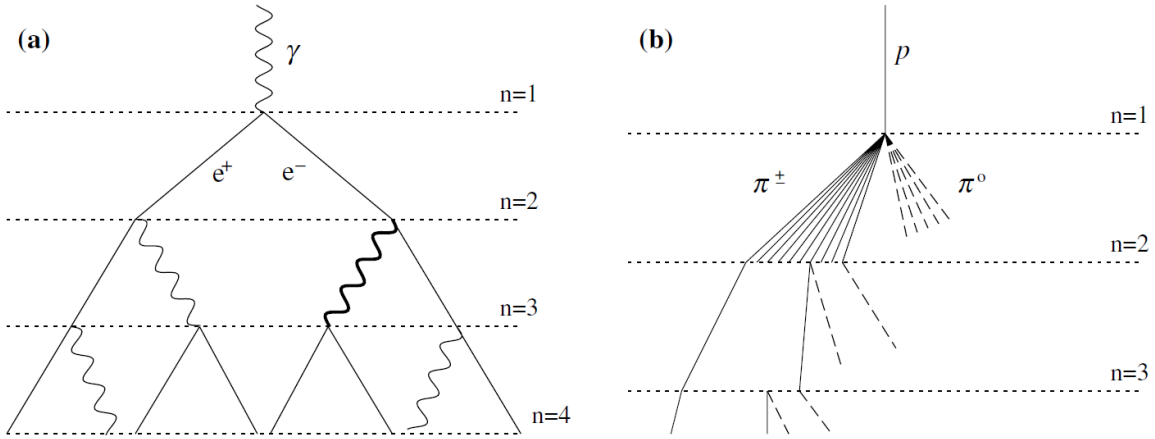

Figure 2.7: (a) Electromagnetic air shower caused by a gamma ray and (b) hadronic air shower caused by the interaction of a proton with the atmosphere (figure taken from [19]).

The radiation length of photons and electrons in air is $X_0 = 36.66\,\mathrm{g/cm^2}$ which is equal to almost one twenty-seventh of the column density of the atmosphere, which lies at $1000\,\mathrm{g/cm^2}$. Thus, first particle interactions and EAS shower creations already occur at around 15 km-20 km above sea level [10]. For precise investigations regarding EAS showers, especially the ones caused by lower energy primary rays, it is therefore advisable to build the detectors in greater heights to still be able to measure a large amount of secondary particles.

2.3.2 Cherenkov Light

The creation of Cherenkov light is a very important physical phenomenon that is used for the indirect ground-based detection of cosmic gamma rays and also builds the base for the detection method that is used in this thesis.
If a particle is travelling through a medium with a velocity that is higher than the speed of light in that medium, Cherenkov light is emitted. It can be described by

$$v \geq \frac{c}{n} \tag{2.9}$$

with v the speed of the particle, c the speed of light and n the refraction index of the medium through which the particle travels. The Cherenkov light, which appears as blue light, is emitted in a cone-like form. Its opening angle θ_{cone} can be calculated using

$$\theta_{\mathrm{cone}} = \arccos \frac{c}{nv}. \tag{2.10}$$

The process which is responsible for the production of the Cherenkov light is explained in the following. When passing through a medium, moving particles briefly generate a dipole field in the particles around them because the sudden presence of a particle in a medium must be compensated by its neighbouring particles. In figure 2.8, this is shown for particles slower than the speed of light in a medium (left hand side) and for particles that fulfil the Cherenkov condition in equation 2.9 (middle panel). For slower

particles the distribution of the resulting dipoles is backwards symmetric. All dipoles cancel each other out and no light is emitted. If equation 2.9 is fulfilled, no forward polarisation is present to cancel out the polarised atoms behind the moving particle. The radiation interferes coherently instead, as can be seen on the right panel of figure 2.8, and builds the Cherenkov cone that can be described by equation 2.10 [18].

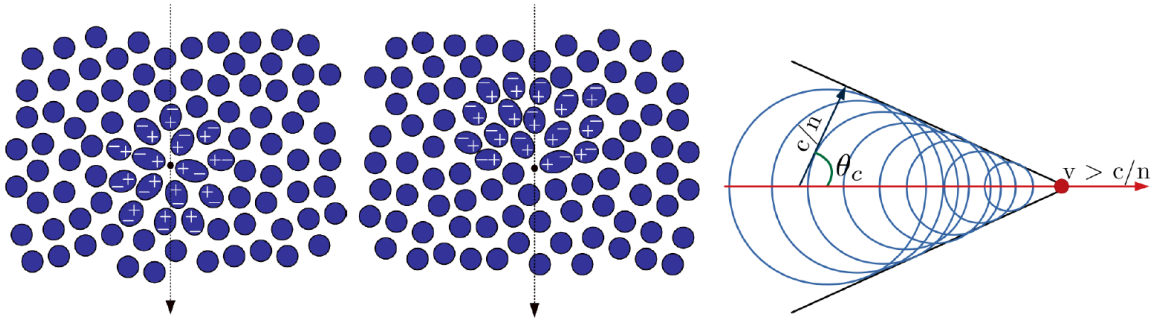

Figure 2.8: Depiction of a particle moving through a medium with a velocity smaller than the speed of light in the same medium (left) and with a velocity greater than the speed of light in the same medium (middle) with the corresponding Cherenkov cone (right) (figure taken from [18]).

Since Cherenkov light is visible light, it can easily be measured with the help of photomultipliers and give information about the characteristics of the original particle. Measuring Cherenkov light is a technique widely used in a multitude of ground-based gamma-ray detection methods, including Imaging Atmospheric Cherenkov Telescopes (IACTs) and water Cherenkov detector (WCD) arrays.

2.3.3 Ground-based Gamma-ray Detection Methods

Over the last two decades in particular, the number of experiments investigating cosmic gamma rays has been increasing enormously. Next to space-based detection methods which are used, for example, at Fermi-LAT[5], a multitude of ground-based detector arrays has been built in recent years. The measurement of Cherenkov light (see section 2.3.2) plays a significant role in many of these observatories today.

In general, the detectors that are used to measure Cherenkov light can vary greatly in their type. On the one hand, large Imaging Atmospheric Cherenkov Telescope (IACT) arrays can be used. Those arrays are made up by a large number of mirror telescopes that reflect the photons from the Cherenkov cones created by the EASs into cameras where they will be recorded. The number of counted photons and the area in which the telescopes have measured a signal provide information about the properties of the primary gamma rays. Detector set-ups using this technique include, for example, the High Energy Stereoscopic System (H.E.S.S.)[13] in Namibia, the Very Energetic Radiation Imaging Telescope Array System (VERITAS)[15] in the US and the Major Atmospheric Gamma Imaging Cherenkov (MAGIC)[7] telescopes in La Palma. Additionally, the Cherenkov Telescope Array (CTA)[2] is planned. It will include a detection site in the Northern as well as the Southern Hemisphere and will observe the whole sky.

Another way to use the Cherenkov technique to measure cosmic gamma radiation is with the help of water Cherenkov detectors (WCDs). In this case, photo sensors are placed within a detector that is filled with water. Secondary particles of an EAS interact with the nuclei in the water and, similar to IACTs, form Cherenkov light that is measured by photo sensors. Two examples for experiments that use WCDs include the High-Altitude Water Cherenkov (HAWC)[9] Gamma-Ray Observatory in Mexico and the Large High Altitude Air Shower Observatory (LHAASO)[6] in China. Since the Cherenkov light may only form in the detector and not in the atmosphere beforehand, the height of the WCD sites must be much higher than the one for sites that use IACTs.
Figure 2.9 shows both a depiction of IACTs and an array using WCDs. For IACTs, the height of the side lies at around 1 km-3 km above sea level while WCD arrays are located at an height of around 4 km-5 km above sea level. On the right hand side of figure 2.9 one can find a zoom in on what such a WCD could look like on the inside. The particle from the particle shower penetrates the tank and interacts with the water, creating a Cherenkov cone that is read out by the photo sensors in the tank.
In general, IACTs are more frequently used for spectral and morphological observations in comparison to WCDs because of their high angular and energy resolution. WCDs have a high-duty cycle of around 100% and a big field of view. Unlike the IACTs, they are not bound to night time or susceptible to specific weather conditions. Since they are closed off, they guarantee measurements at all times. Because of these advantages, WCDs are very useful when investigating extended sources [18].

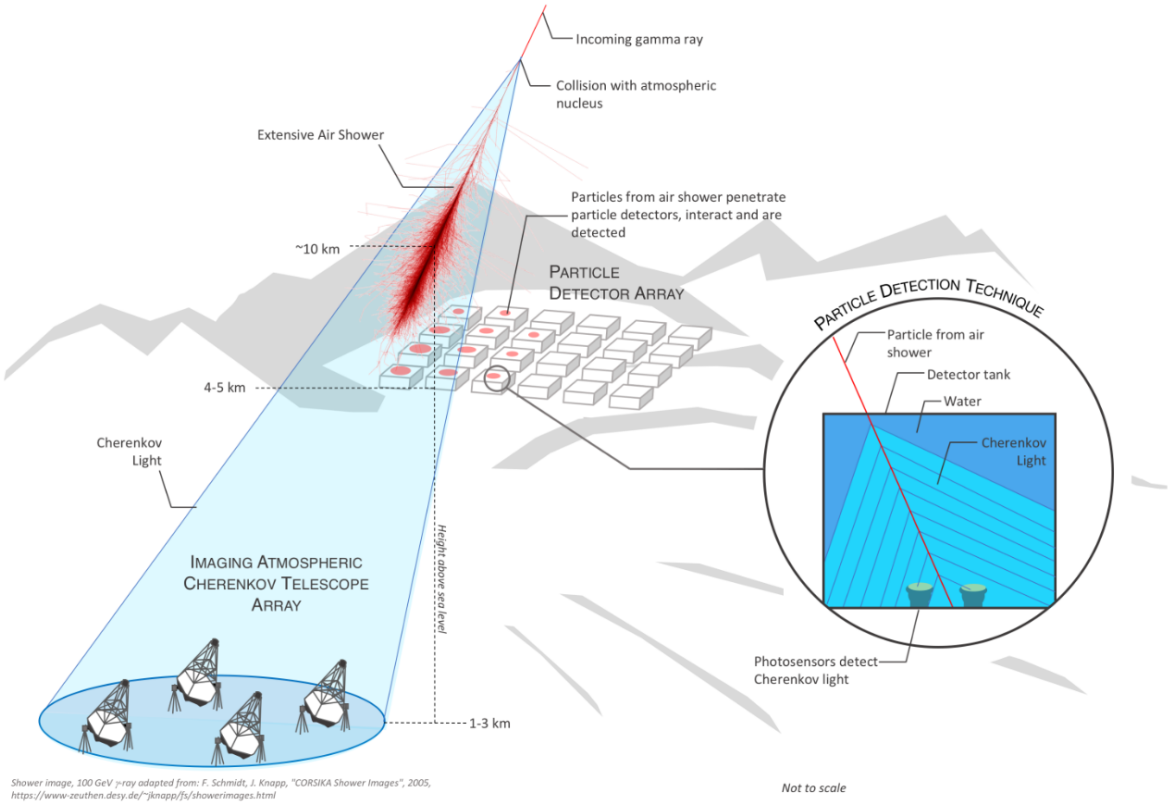

Figure 2.9: Schematic of an IACT and WCD array measuring the Cherenkov light of an EAS that was induced by a primary gamma ray with a close up of the inner workings of a WCD (figure taken from [20]).

Chapter 3

The Southern Wide-field Gamma-ray Observatory (SWGO)

The Southern Wide-field Gamma-ray Observatory (SWGO) will be a new ground-based particle detector array in South America which will investigate gamma rays as well as other cosmic rays from energies of a few tens of GeV to hundreds of TeV. A water Cherenkov detection technique will be used to detect particles for SWGO [14].
The main objectives of SWGO will consist of unveiling and investigating galactic particle accelerators, like the galactic centre and the Fermi bubbles, and monitoring the transient sky like, for example, active galactic nuclei and gamma ray bursts. Furthermore, observations of cosmic rays will be carried out with regard to their spectrum and composition as well as their anisotropy. Physics beyond the Standard Model are also planned. This will, for example, include investigating dark matter, primordial black holes and axion-like particles [4].
The measurements that will be conducted with SWGO can be used both to cross-check previously measured results of its predecessors like HAWC and LHAASO as well as to investigate new sources, especially in regions that are currently undetected. Being located in the Southern hemisphere, it can also complement the future CTA side of the Southern hemisphere [4].
Looking at figure 3.1, a depiction of the planned sky coverage of SWGO is overlaid over a significance map of HAWC. It can be seen that a significant part of the sky that is inaccessible to HAWC will be in the field of view of the future SWGO array.

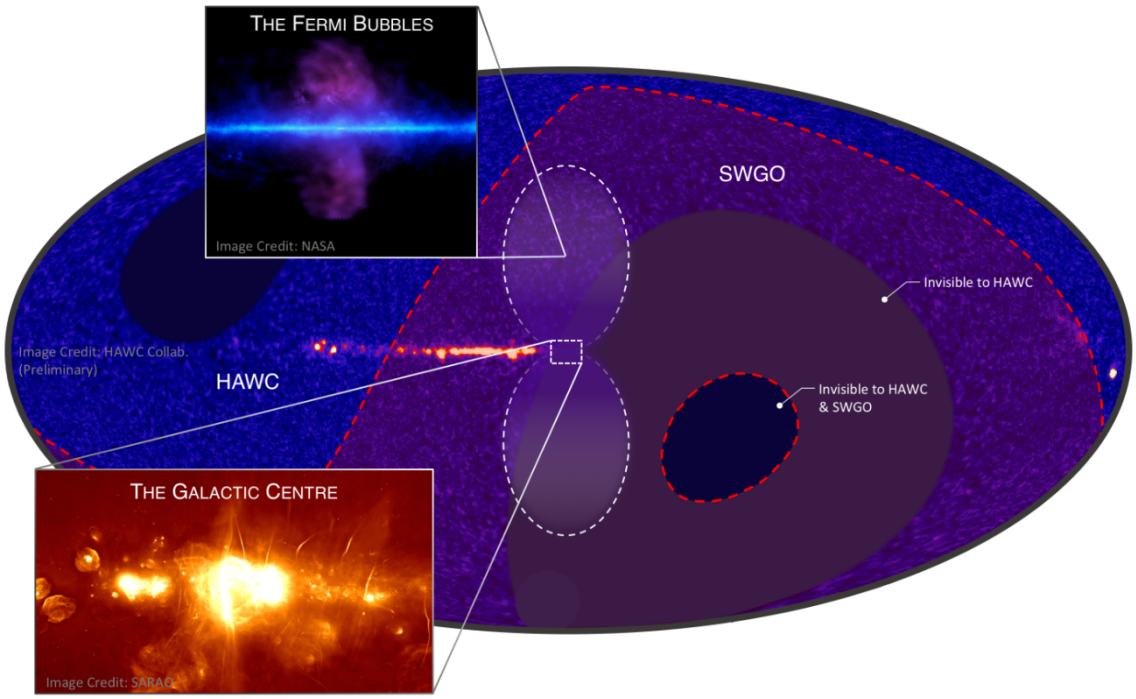

Figure 3.1: Planned sky coverage of SWGO overlaid over a HAWC significance map (figure taken from [14]).

As its successor, the structure and workings of SWGO are motivated by the HAWC array. While the final design of SWGO has not been decided yet, a few baseline propositions for the site have been made. In the following, some of the design propositions that were made in [14] are listed. In this design, the site will consist of a number of double-layered WCD units that are used for the particle detection. The field of view will be approximately 90°. The site location will lie between a latitude of 10° and 40° South at a height above 4500 m above sea level. Whether the detector units will follow a design similar to HAWC, where each WCD unit is represented by a separate tank [9], or a design similar to LHAASO, where all units are placed in a single large volume of water and sectioned off there [6], will also be influenced by the final site location.
A first proposition for a possible layout was given in [4]. It is shown in figure 3.2. This layout consists of a densely packed inner array which covers an area of around 80 000 m^2 and has a fill factor of 80% and a less dense outer array which covers 221 000 m^2 with a fill factor of 8%. For comparison, the size of the HAWC site and its fill factor can also be found in the same figure.

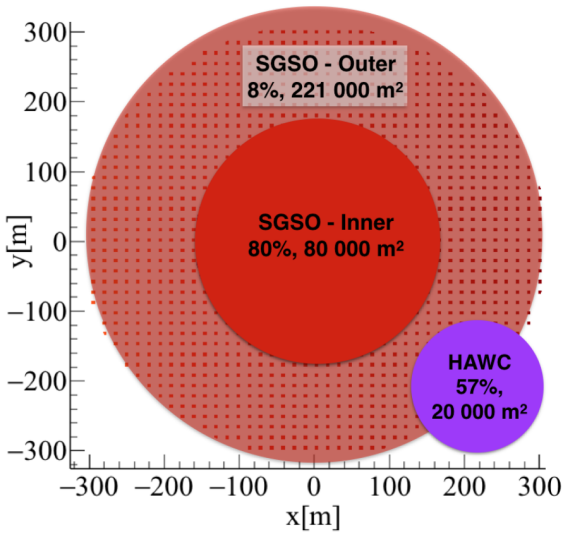

Figure 3.2: First proposition for the SWGO (then Southern Gamma-Ray Survey Observatory (SGSO)[4]) layout compared to the array composition of HAWC. The fill factors and the sizes of the arrays are included (figure taken from [4]).

As mentioned above, the exact layout of SWGO still has to be determined. For this reason, preliminary array layouts are used for the core and energy estimates for SWGO within this work. These preliminary designs are based on the baseline propositions that were mentioned above.
For all preliminary arrays in chapters 5-7, cylindrical double-layer WCD tanks were used as detector units. A depiction of such a tank can be found in figure 3.3. Both the upper cell (UC) and the lower cell (LC) of such a tank contain one photomultiplier tube (PMT) each which is used to measure the Cherenkov light within the cells once a EAS hits the array. The PMT in the UC of a tank is located at the bottom of the cell, centred and points upwards. The PMT in the LC is also centred but it is attached to the ceiling of the cell and points downwards. The exact number and dimensions of the tanks and their distribution within the array differ slightly for each of the preliminary designs that are used for the studies conducted in chapters 5, 6 and 7. They will therefore be stated at a later point when the corresponding evaluations are performed.
All EASs that were used for the studies within this thesis were simulated with the COsmic Ray SImulations for KAscade (CORSIKA)[11] package. The WCD tanks, the interaction of the simulated shower particles with these tanks and the evaluation of these interactions are all simulated with the simulation toolkit Geant4[3].

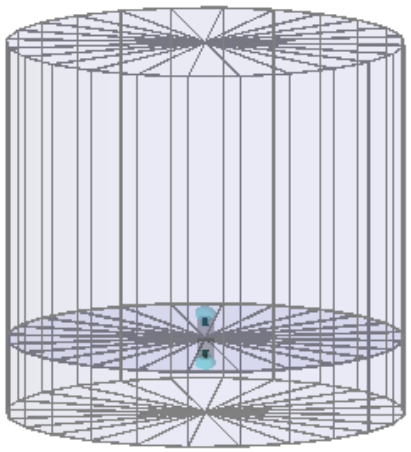

Figure 3.3: General design of a cylindrical, double-layered WCD tank that is used as a detection unit in the preliminary arrays used in this thesis.

Chapter 4

Shower Reconstruction Method

In this chapter, the method which is used to reconstruct the gamma-ray induced air showers for the core and energy estimations conducted in this thesis is explained. This reconstruction method follows the method that was already presented for the HAWC experiment in [17]. It is a template-based reconstruction method which uses a Likelihood approach. The Lateral Distribution Function (LDF) of an incoming gamma-ray induced shower will be reconstructed with the help of templates that were created from Monte Carlo simulations. It can be used to make estimations regarding the core position and the energy of the primary gamma ray.
In the following sections, an explanation of the Likelihood approach will be given, followed by the description of the template generation process. Afterwards, the simulation procedure itself and an example of a reconstructed event will be given.

4.1 Likelihood Method

For the Likelihood approach, the Lateral Distribution Function (LDF) of the EASs is used. It describes the number N_{PE} of observed particles that is measured in a detector unit at a certain distance r from the impact point of the shower core. This information is then used for the estimation of both the reconstructed core position and the reconstructed energy. In general, the LDF of a shower is prone to fluctuate depending on the detector response, the interaction height of the primary particle with the atmosphere and the type of initial primary cosmic ray [18]. Because of this, it is very hard to find an universal distribution that can be used to describe the LDF of a EAS at a certain detection height. While in the following study only gamma-ray induced showers are taken into account, fitting such a shower in an analytical way would still cause many difficulties. With the help of a Likelihood approach it is possible to work around these problems.
At first, templates will be created with the help of Monte Carlo simulations. They depict the LDF of a gamma-ray induced shower in a probabilistic way. Fluctuations can hereby be factored into the model immediately and the LDF will depend solely on the type of detector and no longer on the interaction point of the primary particle with the atmosphere. More details on the template design and generation can be found in section 4.2.

When reconstructing a shower, the LDF of the shower is measured and fitted against the templates. This is done by minimising

$$\log L = -2 \sum_i \log(F(\log_{10}(N_{\mathrm{PE}})_i, r_i, X_{\max}, E|\theta, \phi)) \tag{4.1}$$

which depends on the zenith angle θ and azimuth angle ϕ of the shower. Function F describes the probability that a certain detector unit i measures a logarithmic number of photoelectrons (PEs) ($\log_{10}(N_{\mathrm{PE}})_i$) at a distance r_i from the shower impact point from a shower with a primary energy E and maximum shower depth $X_{\max}$. The perpendicular distance r_i to the shower axis is described by

$$r_i = [(x_i - x_c)^2 + (y_i - y_c)^2 - \sin^2\theta((x_i - x_c)\cos\phi + (y_i - y_c)\sin\phi)^2]^{1/2} \tag{4.2}$$

with x_i, y_i as the position of a detector unit i and x_c, y_c the position of the shower core in the detector plane [17].
The resulting minimised parameters will give an estimation of the energy E of the primary particle that caused the EAS, its core position described by x_c and y_c and its maximum shower depth $X_{\max}$.

Another advantage of this technique is the fact that it can also be applied to arrays that consist of different detector types. One has to simply sum up the log-Likelihoods $\log L_{\mathrm{det},j}$ of each detector type in the array to get the total log-Likelihood function $\log L_{\mathrm{tot}}$ of a mixed detector array [17]. It is

$$\log L_{\mathrm{tot}} = \log L_{\mathrm{det},1} + \log L_{\mathrm{det},2} + \dots . \tag{4.3}$$

For the WCDs that are used for the studies in chapters 5-7, this is especially helpful because the WCD tanks consist of two cells with different geometries (see figure 3.3) and, thus, each cell must be regarded as a different detector type.

4.2 Template Generation

Because of the different geometries of the UCs and LCs of the WCD tanks (see figure 3.3), two sets of templates have to be created. Before filling the templates, all showers have to be binned in energy E, maximum shower depth $X_{\max}$ and incoming zenith angle θ. For each set of parameters (E, $X_{\max}$, θ) a 2D histogram is generated. On the x-axis the templates are binned in the distance r which describes the distance between a tank and the true shower core. On the y-axis the templates are binned in the logarithmic number of PEs $\log_{10}(N_{\mathrm{PE}})$ that was measured in a tank. The z-axis shows the probability P of measuring a certain number of PEs at a certain distance. The probability of measuring no PEs at a certain distance is also saved in the histogram were $\log_{10}(N_{\mathrm{PE}}) = -3$. An example template for one set of parameters (E, $X_{\max}$, θ) for the UCs can be found in figure 4.1a. Figure 4.1b shows the template for the same set of parameters as figure 4.1a but for the LCs.
The size of the binning for E, $X_{\max}$, θ, r and $\log_{10}(N_{\mathrm{PE}})$ as well as their ranges vary for the studies in chapters 5, 6 and 7. For this reason, they will be described in those chapters individually.

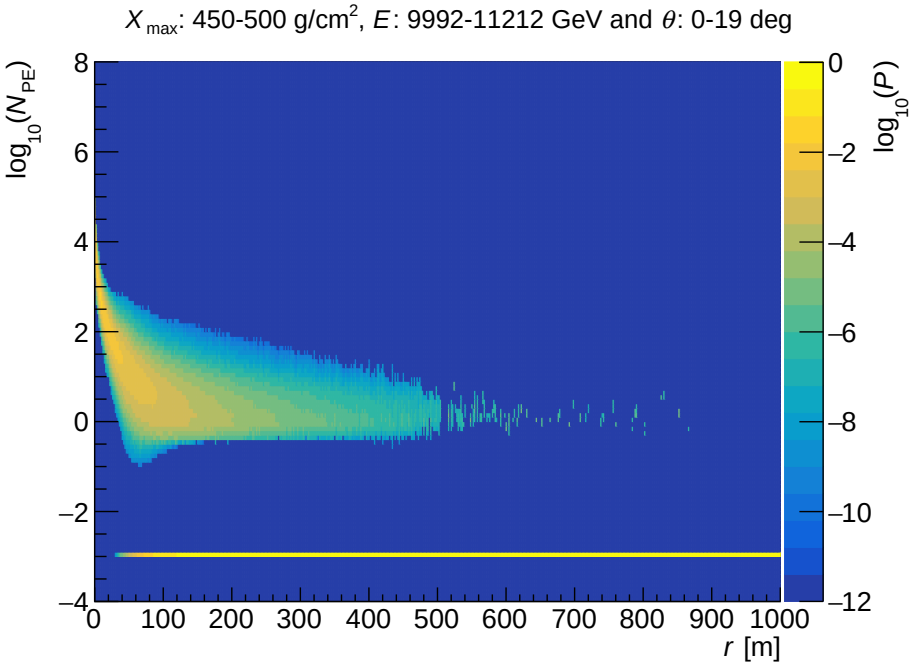

(a) UC template.

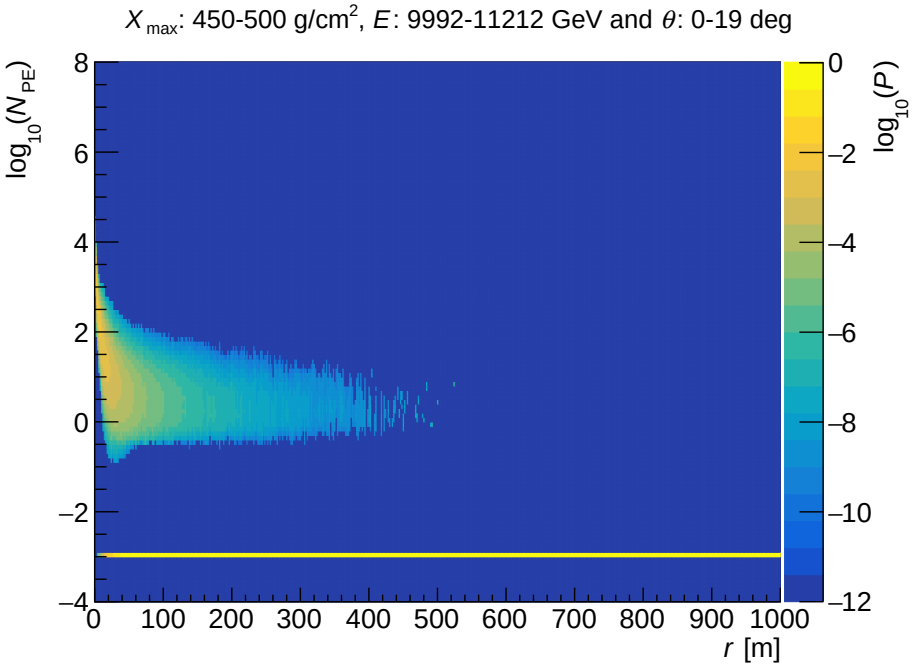

(b) LC template.

Figure 4.1: Monte Carlo generated templates binned in E, $X_{\max}$ and θ as well as in the log-number of observed PEs ($\log_{10}(N_{\mathrm{PE}})$) on the y-axis and the distance r between a tank and the shower core on the x-axis. The z-axis describes the log-probability $\log_{10}(P)$ of measuring a certain number of PEs (N_{PE}) at a certain distance r from the shower core. At $\log_{10}(N_{\mathrm{PE}}) = -3$ the probabitily of measuring zero PEs at a distance r is saved. (a) shows such a template that was generated for the UCs. (b) shows a template for the same set of parameters (E, $X_{\max}$ and θ) that was created for the LCs.

4.3 Template Smoothing

Before the templates can be used for the reconstruction, they have to be smoothed. The templates in figures 4.1a and 4.1b show the final templates after the smoothing process. Figure 4.2 shows an unsmoothed template of the UCs corresponding to figure 4.1a. In the unsmoothed templates, one can find both bins that measure a very low probability P in the middle of the distribution where a higher value would be expected based on their neighbouring bins and ones which show a higher probability even though they are far off from the rest of the distribution, mostly at the very edge of the phase-space. These artefacts arise because it is impossible to cover the entire phase space with simulated Monte Carlo showers while maintaining a reasonable computing time to acquire the necessary amount of showers. To avoid the negative side effects of these artefacts, the templates have to be smoothed. For this, a Gaussian-distributed weighted sum is applied to each bin. The smoothing takes place in both x- and y-direction of the templates.

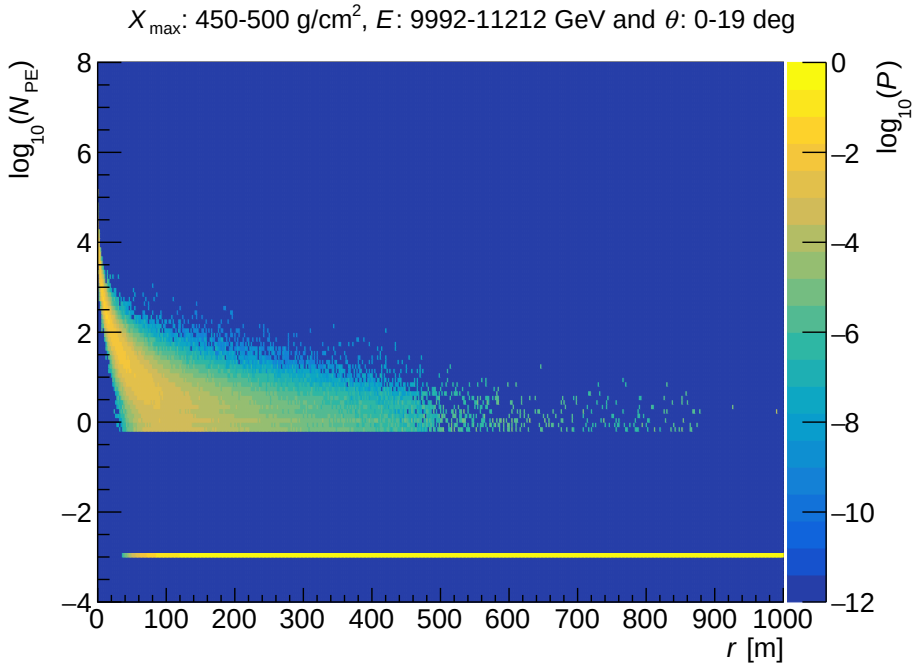

Figure 4.2: Template 4.1a before the smoothing.

4.4 Fitting Procedure

The reconstruction module that is used to reconstruct gamma-ray induced air showers in this thesis operates on fitting the LDF of an EAS to the templates defined in section 4.2 by minimising the log-Likelihood described in section 4.1. The parameters that have to be fitted consist of the core position described by x_c and y_c, as well as the energy E of the shower and the maximum shower depth X_{max} for a specific azimuth angle ϕ and zenith angle θ (see function 4.1). With the help of a 3D-grid interpolation over E, X_{max} and r, one can find the probability to measure any signal $\log_{10}(N_{PE})$ at any

distance r of a tank from the shower core in the templates. This will help to keep the likelihood surface smooth.

Here, it must be pointed out that finding the correct parameters E and $X_{\max}$ of the reconstructed showers is complicated by strong fluctuations of the LDFs. Since the first interaction of a primary particle with the nuclei in the atmosphere is not fixed at a certain height, the signal that is measured in the WCD tanks can differ greatly from shower to shower even for gamma-ray induced showers with the same primary properties. This leads to an ambiguity between E and $X_{\max}$ in the reconstruction that cannot be eliminated completely, it can only be alleviated [17].

Before the fitting process can begin, a starting value for E, $X_{\max}$, x_c and y_c and the incoming angles ϕ and θ has to be determined. The energy can be estimated by counting the number of tanks on the array that measured at least a single hit (N_{hit}) for showers with a certain distance between their trial shower core and the centre of the array. The corresponding histogram that is used for this guess is shown in figure 4.3. It was filled with the help of Monte Carlo simulations.

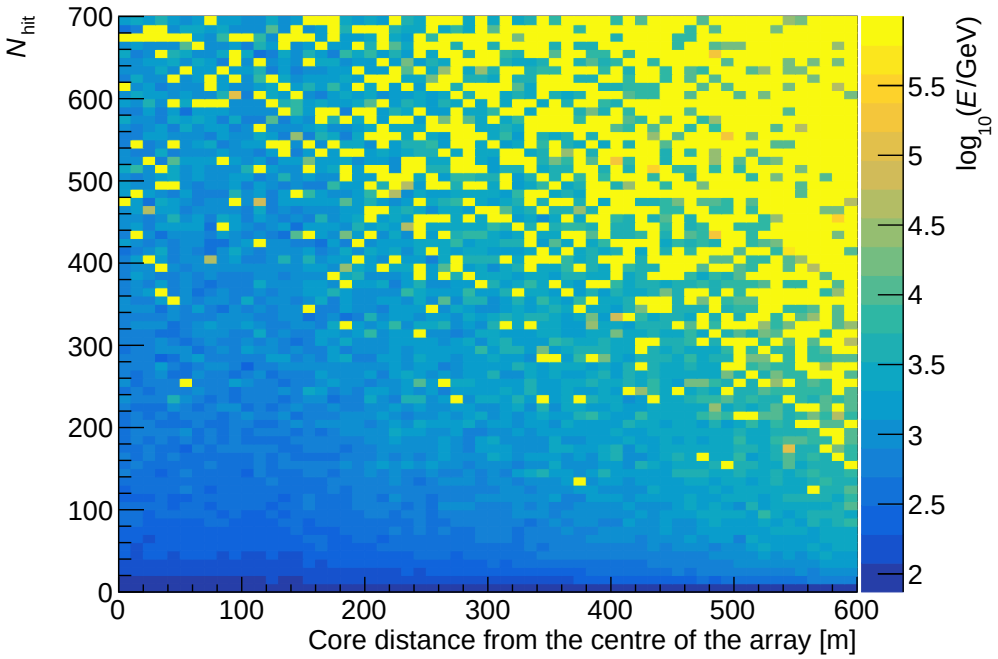

Figure 4.3: Energy guess as a relation between the number of tanks N_{hit} that measured a signal and the distance between the shower core and the centre of the array.

After the starting value for the energy has been estimated, the $X_{\max}$ guess can be determined by using figure 4.4 which shows the relation between $X_{\max}$ and the true energy E that could be obtained from Monte Carlo simulations. To alleviate the above mentioned ambiguity between E and $X_{\max}$, a linear relation between E and $X_{\max}$ is derived from the Monte Carlo simulations.

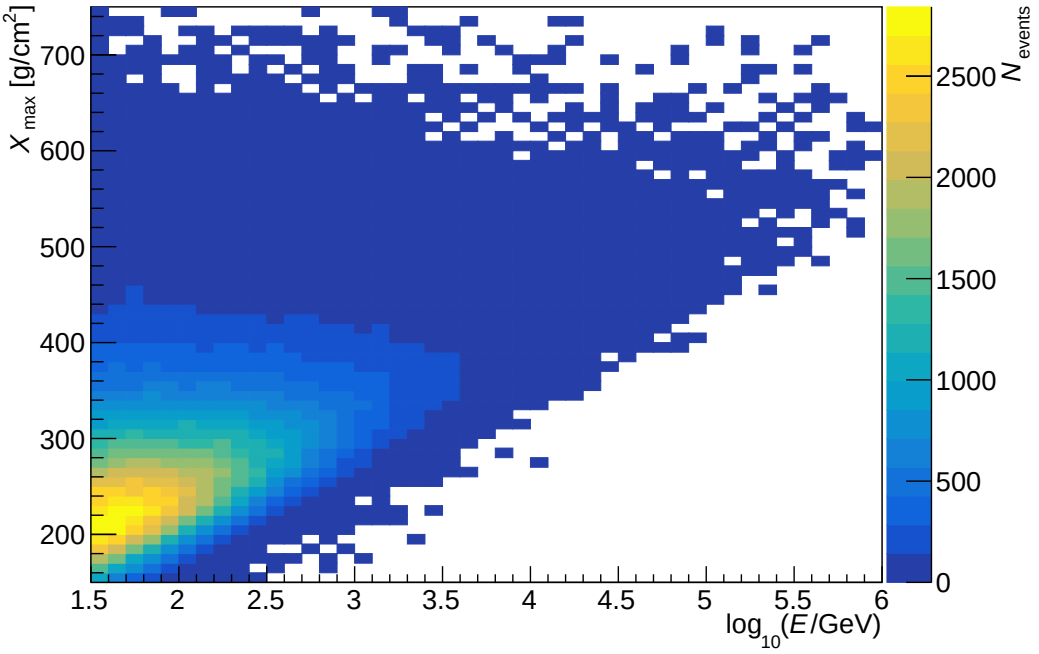

Figure 4.4: Relation between $X_{\max}$ and the true energy E_{true} for a number of Monte Carlo simulated showers.

While the starting values for E and $X_{\max}$ are calculated within the same module which is used for the reconstruction of the showers, the starting values for the angle and core are taken from separate modules of the SWGO software framework. For this reason, the estimation of the initial core and direction will only be briefly summarised here. A more in depth description can be found in [18].
For the core guess, the centre of mass (COM) of the incoming shower is calculated using the charge that was measured within each cell. The COM shower core can then be used to calculate the angle guess. The angle guess is defined through a curved shower front fit. It uses the arrival time at which a signal was measured within a cell to fit the disk-like shower front of an incoming EAS. Depending on the arrival times that are measured in the cells surrounding the core of a shower, the shower direction can be determined.

Once the starting values are acquired, the minimisation is conducted with a fixed number of iterations with the help of the MINUIT minimisation algorithm [16]. For the reconstruction performed in this thesis, the number of iterations was set to 10 to preserve a reasonable computation time. In addition, the minimisation was repeated for multiple core guesses to ensure that local minima as a result of the minimisation are avoided. As mentioned above, the first starting value for the core position is the calculated COM. The other starting values, also called trials, were chosen to be in line with the centre of the array and the COM. Because the COM will always fall on the array, at least one of the trial locations should lie outside of the array. Furthermore, trial points must also be set at locations where the tank distribution of the layout changes, as the COM calculation is strongly influenced by the tank density of the array.

After conducting a minimisation at each of the mentioned trial locations, the best fit values of those minimisations are used as the final values.

For the studies conducted in this thesis, the true shower angle was used instead of using the angle fitter that was mentioned above because, at that time, only a preliminary un-optimised angle fitter was available, which is still a work in progress. However, this does not significantly affect the results, as the binning of the templates in the zenith angle is relatively sparse. As long as the future angle fitter can resolve angles within a few degrees, which is true for WCD arrays such as HAWC [1], similar results can be expected.

4.5 Reconstruction of an Example Event

In the following, an example event was reconstructed by using the templates and reconstruction method described throughout chapter 4. The true energy of the primary gamma ray that was reconstructed was $E_{\text{true}} = 10740\,\text{GeV}$. Its true maximum shower depth was $X_{\text{max,true}} = 432\,\text{g/cm}^2$. It was thrown at $x_{\text{true}} = -104.3\,\text{m}$ and $y_{\text{true}} = 143.8\,\text{m}$ from the array centre. Figures 4.5 and 4.6 show the corresponding template of the UCs and LCs to which the example shower was fitted.
Comparing the true shower properties with the binning in figures 4.5 and 4.6, shows that the energy and X_{max} of the shower were fitted to the correct template. The exact values for the reconstructed energy and X_{max} lie at $E_{\text{rec}} = 10593\,\text{GeV}$ and $X_{\text{max,rec}} = 436\,\text{g/cm}^2$ which means the reconstructed values agree with the true values reasonably well.
In this case, the probability to measure zero PEs (P_0) in a tank is not shown in the 2D plots like in the templates in figures 4.1a and 4.1b, but in an extra 1D histogram. Through this, the LDF of the shower can be depicted better for this example. Each dot in the 2D histograms symbolises a tank that is located at a distance r from the shower core and measured a certain number of PEs (N_{PE}). The vertical lines in the 1D histograms symbolise tanks that measured no signal at a certain distance r from the shower core.

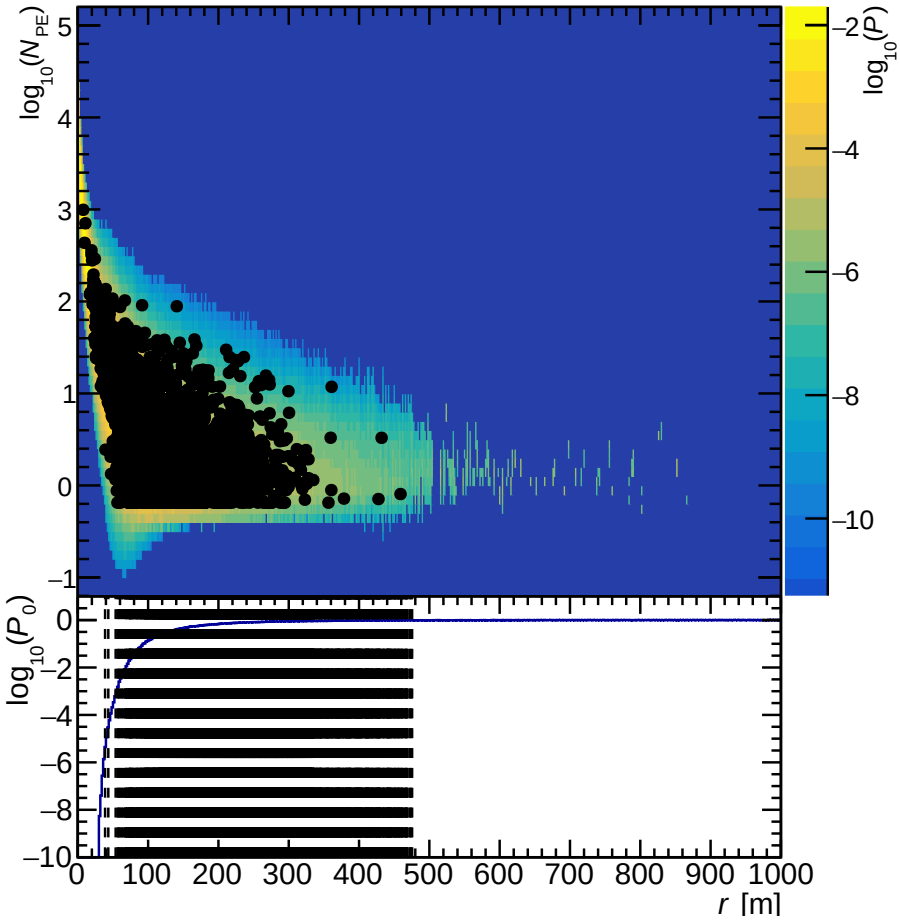

Figure 4.5: UC template binned in energy $E = 9992\,\text{GeV}$-$11212\,\text{GeV}$, $X_{\text{max}} = 400\,\text{g/cm}^2$-$450\,\text{g/cm}^2$ and $\theta = 0°$-$19°$. The primary gamma ray was described by $E_{\text{true}} = 10740\,\text{GeV}$ and $X_{\text{max,true}} = 432\,\text{g/cm}^2$. The reconstructed values lie at $E_{\text{rec}} = 10593\,\text{GeV}$ and $X_{\text{max,rec}} = 436\,\text{g/cm}^2$. The LDF of the shower is also included in the plot. The black dots show the tanks that measured a signal while the vertical lines in the 1D histogram symbolise the tanks that measured no signal.

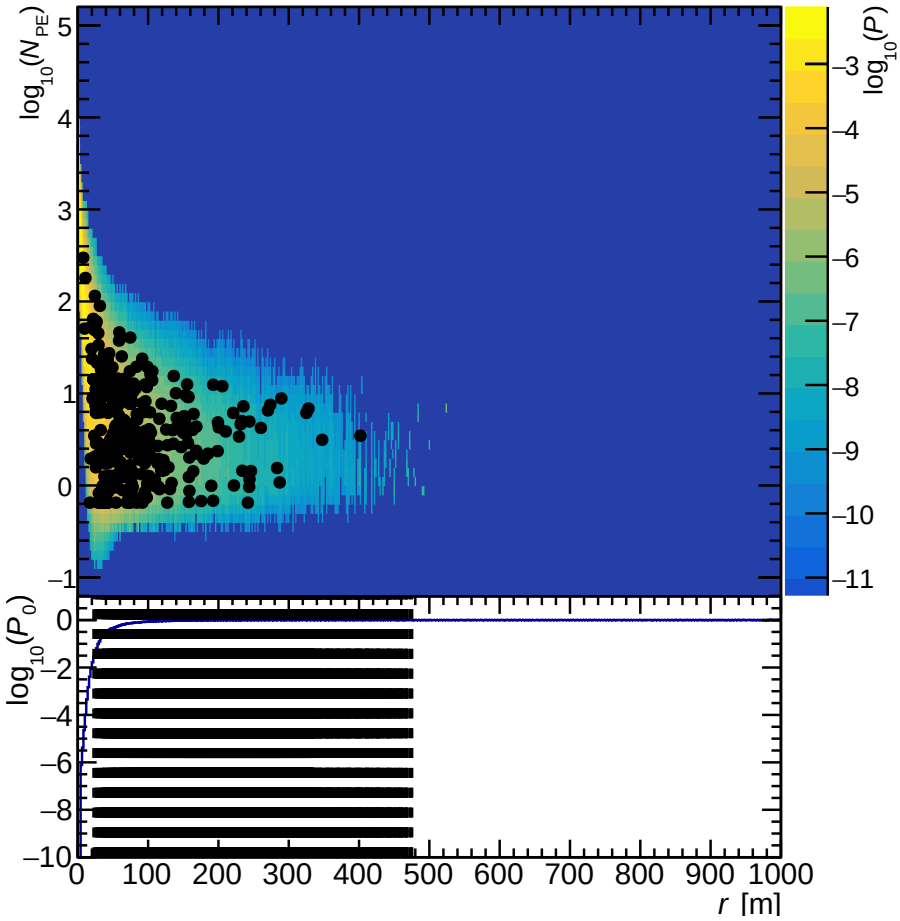

Figure 4.6: LC template binned in energy $E = 9992\,\text{GeV}$-$11212\,\text{GeV}$, $X_{\text{max}} = 400\,\text{g/cm}^2$-$450\,\text{g/cm}^2$ and $\theta = 0°$-$19°$. The primary gamma ray was described by $E_{\text{true}} = 10740\,\text{GeV}$ and $X_{\text{max,true}} = 432\,\text{g/cm}^2$. The reconstructed values lie at $E_{\text{rec}} = 10593\,\text{GeV}$ and $X_{\text{max,rec}} = 436\,\text{g/cm}^2$. The LDF of the shower is also included in the plot. The black dots show the tanks that measured a signal while the vertical lines in the 1D histogram symbolise the tanks that measured no signal.

Figure 4.7 shows the array on which the example shower was reconstructed as well as a close up on the area surrounding the reconstructed core. The black dots depict the tanks of the array. If a charge was measured in the UCs, the corresponding tank is lined in violet, if the LCs measured a charge, then the corresponding tank is lined in pink. The trial points that were used in the fitting process (see section 4.4) are marked in brown. The Likelihood surface is drawn both in the image of the whole array and the close up. The surface goes from the maximum of the log-Likelihood (red) to the minimum (blue). The reconstructed shower core, marked as a green star, can be found in the minimum of the likelihood surface at $x_{\text{rec}} = -102.7\,\text{m}$ and $y_{\text{rec}} = 144.4\,\text{m}$ which indicates a reasonably well core reconstruction for a shower with a true core at $x_{\text{true}} = -104.3\,\text{m}$ and $y_{\text{true}} = 143.8\,\text{m}$.

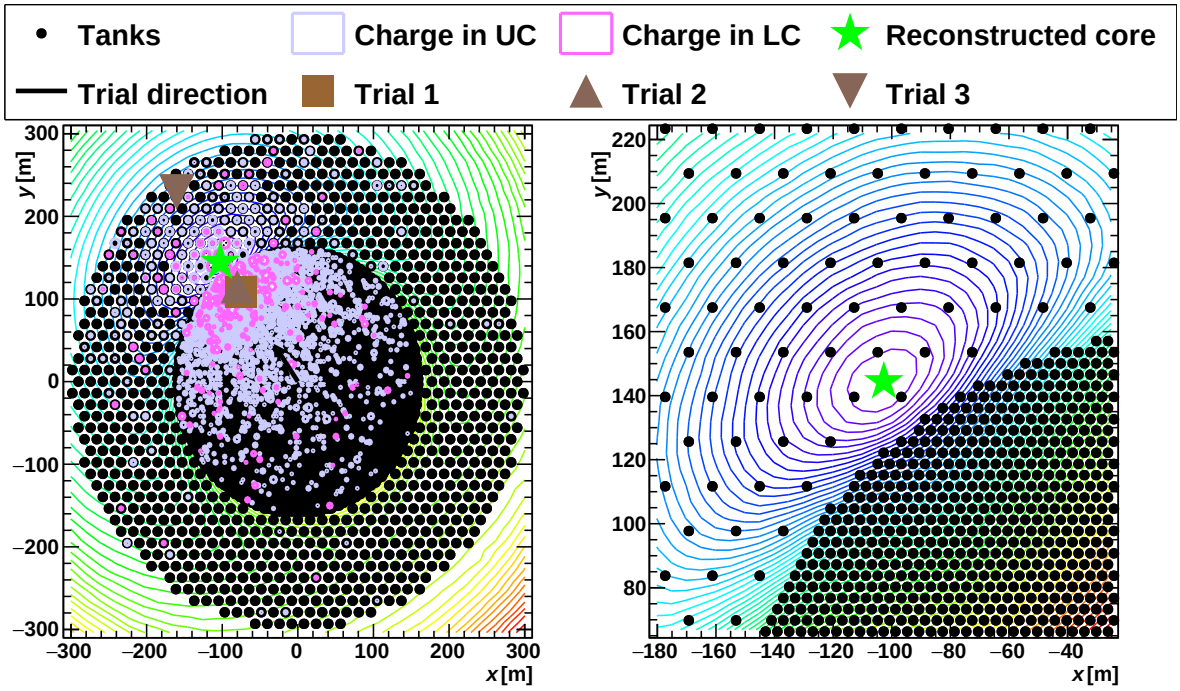

Figure 4.7: Detector array with reconstructed shower at $x_{\text{rec}} = -102.7\,\text{m}$ and $y_{\text{rec}} = 144.4\,\text{m}$ and likelihood surface. The likelihood surface goes from the maximum (red) to the minimum (blue). A close up of the area surrounding the reconstructed core can be seen on the right. The true location of the core was at $x_{\text{true}} = -104.3\,\text{m}$ and $y_{\text{true}} = 143.8\,\text{m}$.

Chapter 5

Test Array Layout

In the following chapter, the performance of the reconstruction module is tested for the first time for SWGO. A test array is used to investigate how the use of different cells and the reconstruction of showers with different angles of incidence influence the core and energy estimations. However, before the investigations regarding the cells and the angles of incidence are conducted, the design of the test array is described. Finally, a bin optimisation is carried out to find the best bin sizes for the templates.

5.1 Test Array Layout and Shower Simulations

The test layout was designed taking into account the proposals for the future configuration of SWGO given in chapter 3. Figure 5.1 shows the test array from above. The array is located at a height of 4700 m above sea level. The layout of the array consists of a dense inner array and a sparser outer array. The radius of the inner array is $r_{\mathrm{i}} \approx 160\,\mathrm{m}$ and the radius of the outer array $r_{\mathrm{o}} \approx 300\,\mathrm{m}$. The WCD units that are used for this array are placed in a square grid structure where the outer walls of the tanks in the inner array touch their neighbouring tanks. Overall 4873 tanks are used to fill the inner array, giving the inner array a fill factor of $f_i = 76.54\%$. 1404 tanks are placed in the outer array which leads to a fill factor of $f_o = 7.98\%$ for the outer array. The tanks themselves are cylindrical, double-layered WCDs with one PMT in each cell, as described in chapter 3. The PMT of the UC is located at the bottom of the cell and facing upwards, while the one in the LC is fixed on the ceiling of the cell and facing downwards. The geometric characteristics of the tanks are described more in detail in table 5.1.
The showers that are used for the generation of the templates and the reconstructions have a primary energy between 31.6 GeV and 1 PeV. The binning of the templates can be found in table 5.2. Only showers with a zenith angle of $\theta_0 = 0°$ and $\theta_{45} = 45°$ are used for the studies within this chapter. The showers with θ_0 are filled in separate templates from the ones with θ_{45}. For this reason, no specific zenith angle binning is necessary. Vertical showers are only reconstructed with the templates that were generated with vertical showers and the same applies to the showers with θ_{45}.
All showers were thrown on the inner array of the test configuration and at least 15 tanks had to be triggered so that a shower could be reconstructed.

Characteristics	Upper Cell	Lower Cell
radius [m]	2.0	2.0
height [m]	3.0	0.75
thickness [mm]	6.0	6.0
inner lining	tyvek	tyvek

Table 5.1: Geometry of the double-layered WCDs used in the test array.

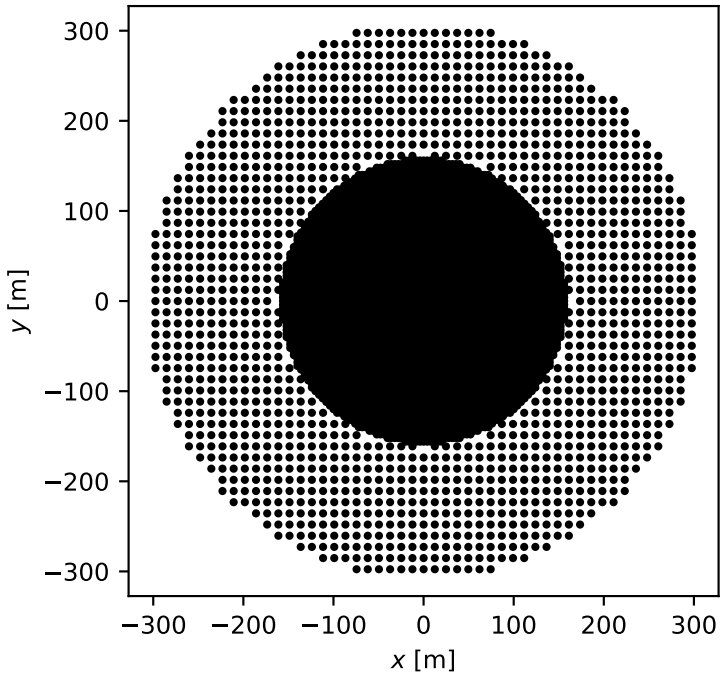

Figure 5.1: Test array layout consisting of a dense inner array and a sparser filled outer array.

Parameters	Range	Bin Size	Description
E	31.6 GeV to 1 PeV	0.3	binned in $\log_{10}(E/\mathrm{GeV})$
X_{max}	150 g/cm^2 to 750 g/cm^2	150 g/cm^2	-
r	0 m to 700 m	2 m	-
$\log_{10}(N_{\mathrm{PE}})$	-4 to 8	0.1	binned in $\log_{10}(N_{\mathrm{PE}})$

Table 5.2: Binning of the energy E, maximum shower depth X_{max}, distance r between the tanks and the shower core and measured signal $\log_{10}(N_{\mathrm{PE}})$ of the templates that are used to reconstruct showers with the test array.

5.2 Core and Energy Estimation

In this section, the core and energy estimations for the test array are conducted. At first, the performance of the reconstruction of vertical showers is tested. For this, core

and energy estimations are performed twice. One time only the UCs of the tanks are used for the reconstruction and the second time both cells are used to investigate the influence of the additional LCs on the performance. Afterwards, this is repeated for the showers with zenith angle θ_{45} and compared to the results of the vertical showers to evaluate how higher zenith angles affect the reconstruction.

5.2.1 Upper and Lower Cells

Because the template-based reconstruction method of chapter 4 has only been tested for single-layered tanks at HAWC [9][17], the influence of additional LCs in the detection units that are used for SWGO is evaluated in the following. Showers are first reconstructed using only the UCs of the tanks. Then, they are reconstructed using both cells. The results of the two methods are compared afterwards. In this section, only vertical showers are tested since the LDF of a shower strongly depends on the incoming zenith angle. Showers with a bigger inclination could further influence the test results. By testing the module only for vertical showers, this additional influence can be neglected and the effect of the additional LCs can be investigated more clearly.

Core Estimation

To evaluate the core reconstruction, the distance d between the reconstructed and the true shower core of all reconstructed showers is plotted for different energies. Figures 5.2a and 5.2b show the results for reconstructing showers while using only the UCs and the UCs and LCs together, respectively.

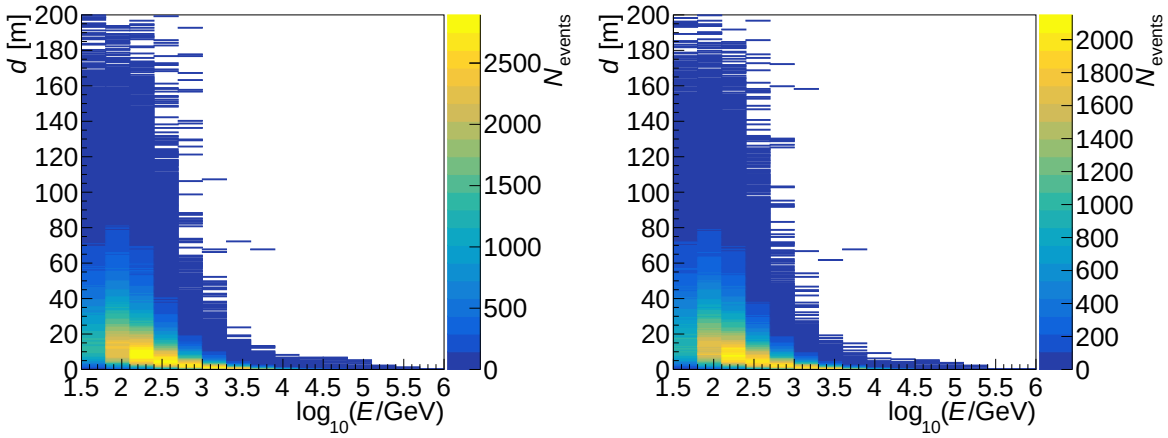

(a) (b)

Figure 5.2: Distance d between the reconstructed and the true shower core of the reconstructed showers for different energies while (a) using only the UCs and (b) using both cells for the reconstruction.

With the help of figures 5.2a and 5.2b, one can estimate the core reconstruction by calculating the core resolution. It is defined as the 68% containment radius of the distribution of the distance d between the reconstructed and true shower core for each

energy bin. The results, both for using only the UCs and using the UCs and LCs together, are shown in figure 5.3.

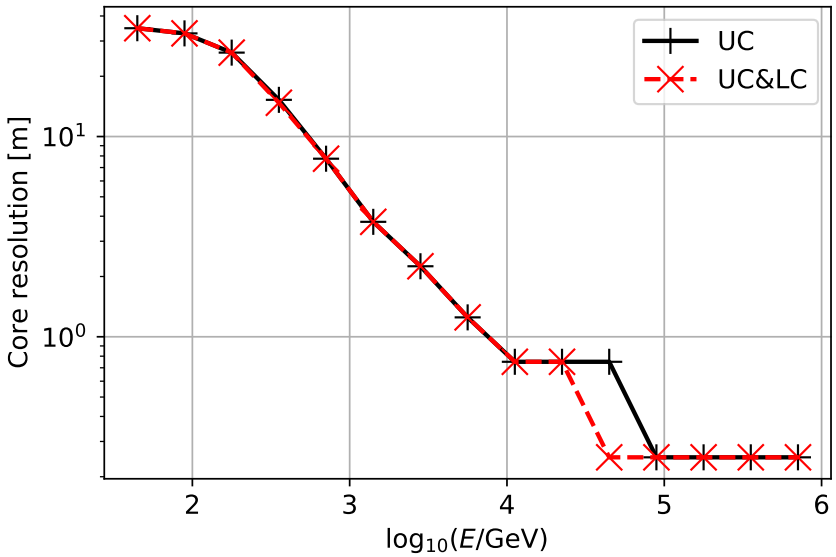

Figure 5.3: Core resolution at different energies for reconstructing showers using only the UCs and using the UCs and LCs together.

Looking at figure 5.3, one can find that the core resolution improves with increasing energy. At an energy in the order of 10^3 GeV, the core resolution is already below 10 m. For energies in the order of 10^4 GeV and higher, the core resolution is below 1 m. If the shower-inducing primary gamma-ray has a higher energy, the number of particles created in the EASs is higher. In addition, the particles have a higher chance to reach the detector array without loosing all their energy first. This leads to a higher number of triggered tanks. With a higher number of tanks triggered, the performance of the reconstruction improves because there is more information which can be used to constrain the likelihood value (see equation 4.1) and, thus, the fit (see section 4.4). This, in turn, leads to a better core resolution.
Comparing both graphs, one can find that the core resolution is very similar in both cases. Only at an energy of $E = 10^{4.65}$ GeV, a different resolution can be found which is most likely a statistical artefact. It seems like using the additional LCs does neither worsen nor improve the results for reconstructing vertical showers significantly when it comes to the core resolution.

Energy Estimation

One way to evaluate the energy estimation of the showers is to plot an energy dispersion matrix (see figure 5.4). There, the reconstructed energy E_{reco} of the showers is plotted over their true energy E_{true}. If the energy dispersion matrix shows a diagonal distribution, the events are reconstructed correctly. Comparing the energy dispersion matrix when reconstructing showers with only the UCs (see figure 5.4a) and using both cells (see

figure 5.4b), a diagonal trend can be found in both. Again, no significant difference between both cases can be found.

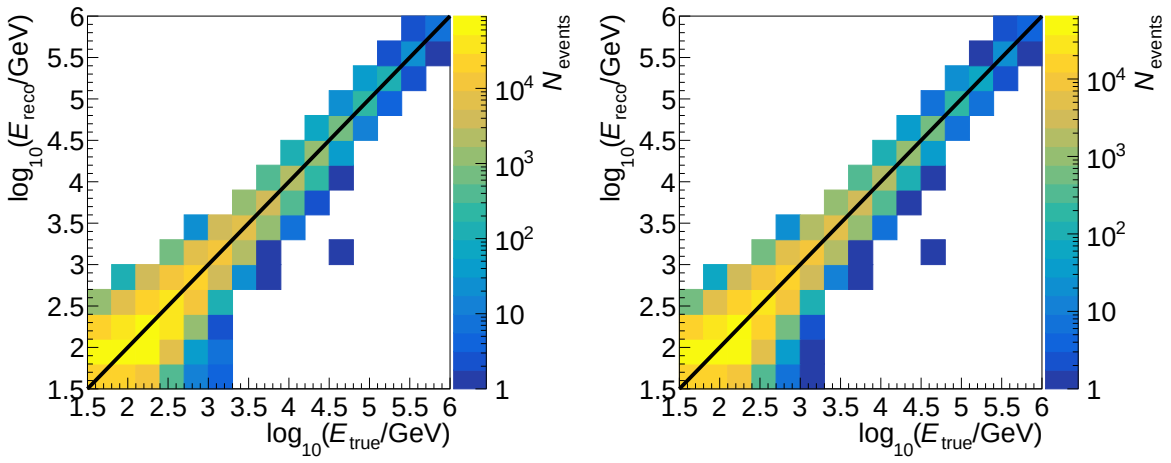

(a) (b)

Figure 5.4: Energy dispersion matrix for reconstructing showers with (a) the UCs only and (b) the UCs and the LCs together.

Another way to characterise the energy estimation is to plot the energy bias and energy resolution. To acquire both values, the difference $(\log_{10}(E_{\text{reco}}/\text{GeV}) - \log_{10}(E_{\text{true}}/\text{GeV}))$ between the true energy E_{true} and the reconstructed energy E_{reco} has to be plotted for each energy bin and all reconstructed showers. Figure 5.4 shows the results for reconstructions with the UCs and the UCs and LCs together. The energy bias can be obtained by calculating the mean of $\log_{10}(E_{\text{reco}}/\text{GeV}) - \log_{10}(E_{\text{true}}/\text{GeV})$ in figure 5.5 for each energy bin. The energy resolution is defined as the Root Mean Square (RMS) of $\log_{10}(E_{\text{reco}}/\text{GeV}) - \log_{10}(E_{\text{true}}/\text{GeV})$ of each energy bin. Comparing the results of the energy bias (see figure 5.6) and the energy resolution (see figure 5.7) for using the UCs only and using both cells together, one can find that the difference between both graphs is neither significant for the energy bias nor for the energy resolution.
For lower energies below and in the order of 100 GeV, the values of the energy bias and resolution are quite high. For higher energies a better bias and resolution can be estimated. Again, this behaviour can be explained by the higher number of particles that is caused by the higher energy EASs which trigger more tanks and, thus, improve the fitting process. A spike in both the energy bias and resolution can be seen between 10^5 GeV and 10^6 GeV. It is most likely caused by the low statistics of high energy showers. The templates for these energies are filled less which, in turn, leads to a less precise reconstruction.

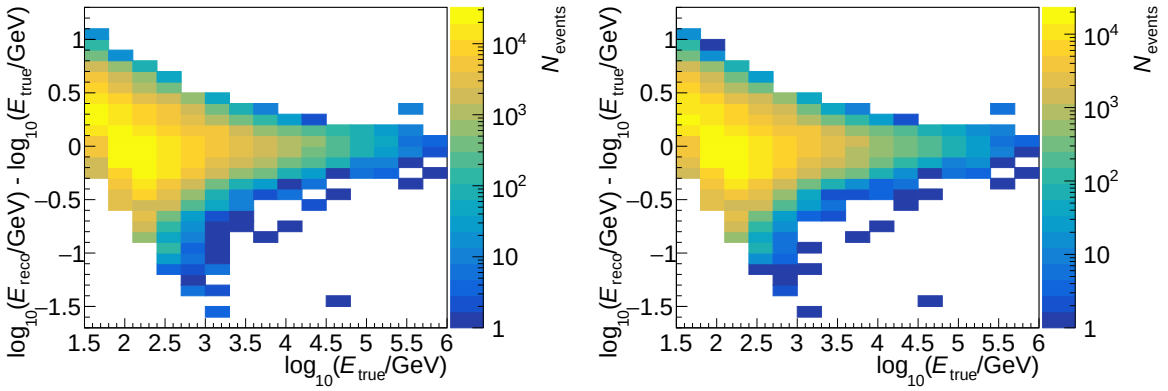

Figure 5.5: Difference between the true energy E_{true} and the reconstructed energy E_{reco} for reconstructing showers with (a) the UCs only and (b) the UCs and the LCs.

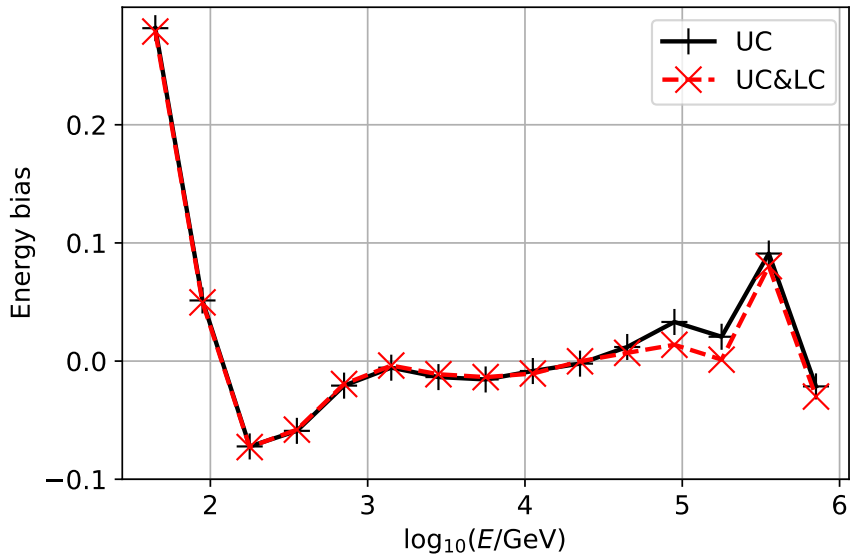

Figure 5.6: Energy bias when using only the UCs and using both cells for the reconstruction.

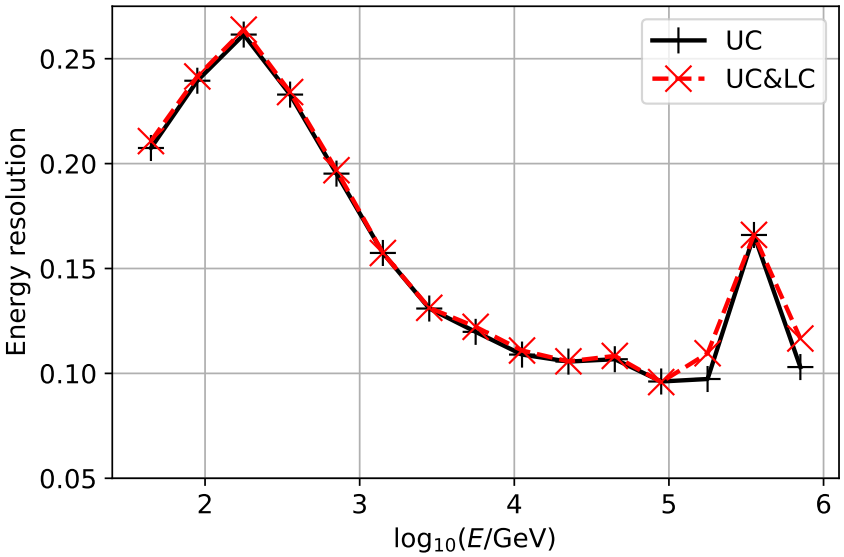

Figure 5.7: Energy resolution when using only the UCs and using both cells for the reconstruction.

Summarising the results of the core and energy estimations that were conducted for the test array, one finds that the use of the additional LCs in the reconstruction does not influence the results in regards to the core resolution, energy bias and energy resolution that could be attained when reconstructing vertical showers. This means that, in this case, using the additional LCs to evaluate the core and energy estimations is not necessary.
However, it has to be taken into account that the PMTs used in the simulations are implemented without a saturation threshold so far. Since the LCs are mostly shielded from direct contact with the showers by the UCs, they do measure a lot less PEs. This means that a saturation of the LCs can be assumed to happen less likely than one of the UCs. In real life, PMTs without a saturation threshold can not be realised which means a value has to be set in the future.
The cells which include a saturated PMT have to be excluded from the reconstruction bringing down the number of tanks that measured a signal and, therefore, worsening the final results. If the LCs are used in addition to the UCs, once such a saturation threshold is implemented, the loss of information through saturation is smaller which will have a positive effect on the reconstruction. Once the simulations also take the saturation of a PMT into account, a positive effect on reconstructing showers with the additional LCs is expected. Investigations regarding the influence of the LCs when the saturation of PMTs is considered are planned for the future.

5.2.2 Shower Reconstruction with θ_0 and θ_{45}

Next, it was tested how the reconstruction results of showers with a higher incoming zenith angle $\theta_{45} = 45°$ compare to those of vertical showers with θ_0. For this, two sets

of templates were created. The template set that is used to reconstruct the vertical showers was only filled with vertical showers. The same was applied to the showers with θ_{45}.
In addition, the results are again compared for reconstructions that were conducted while using only the UCs and using the UCs and the LCs together.

Core Estimation

The core estimations for reconstructing showers with different θ and different cells are shown in figure 5.8. The additional use of the LCs in the reconstruction does, once more, not seem to make a significant difference even when reconstructing showers with a bigger inclination.
The general trend of a decreasing core resolution for higher energies also seems to apply for reconstructing showers with θ_{45}.
Comparing the core resolution of the vertical showers with the ones with θ_{45}, one can see, that the values of the core resolution are a lot higher for higher zenith angles. When a particle shower has a higher zenith angle, the distance it has to travel through the atmosphere before it reaches the detector array is bigger than for vertical showers which means the shower loses more energy on its way and the number of particles at the detection height is much lower. As explained in 5.2.1, this will influence the fitting process negatively, leading to a worse core resolution.

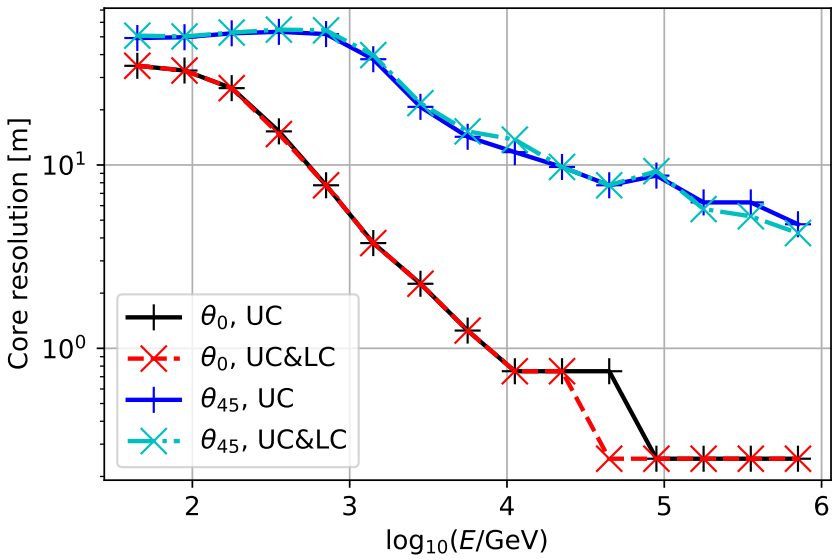

Figure 5.8: Core resolution at different energies for reconstructing showers with θ_0 and θ_{45} using the UCs only and the UCs and LCs together.

Energy Estimation

Concerning the energy estimation for higher zenith angles, one can also see that the results worsen for θ_{45}. The energy dispersion matrix of reconstructed showers with a zenith angle θ_{45} (see figure 5.9b) is broader than the one for vertical showers (see figure

5.9a). The distribution for showers with an inclination of θ_{45} is also shifted slightly from the diagonal and the reconstructed values do not start below energies in the order of 100 GeV.

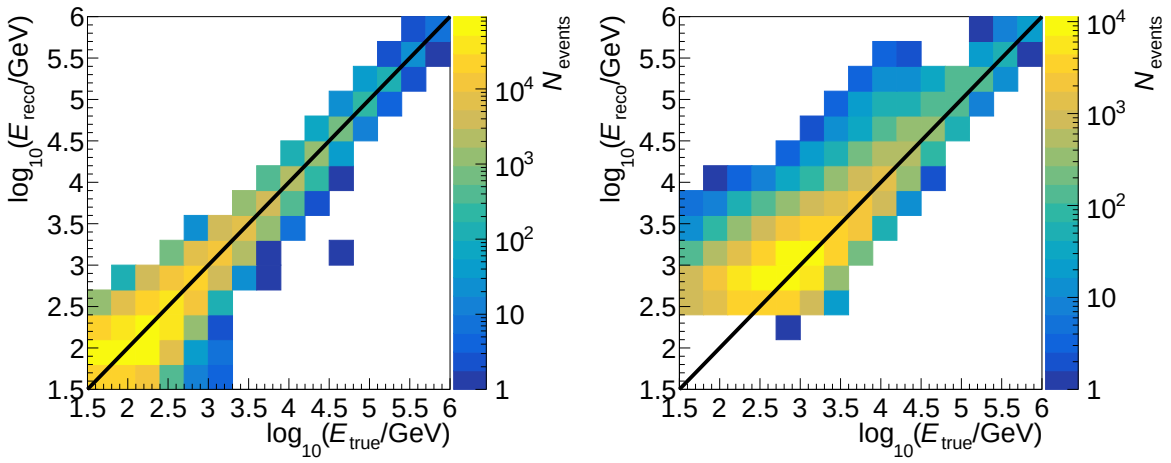

Figure 5.9: Energy dispersion matrix of the test layout using (a) vertical showers and (b) showers with a zenith angle of $\theta = 45°$ for the reconstruction. The reconstruction was conducted using only the UCs in both cases.

The results for energy bias and energy resolution are also worse for θ_{45}. While the energy bias (see figure 5.10) is quite high for lower energies, it does reach similar values to the ones obtained with the vertical showers after energies in the order of 10^3 GeV. The energy resolution almost continuously lies above the one for vertical showers (see figure 5.11).

Regarding the performance of the core and energy estimations for showers with θ_{45}, it can be seen that, similar to the studies with vertical showers, the additional use of the LCs does not make a significant difference since no saturation effect is taken into account as of now. For this reason, all studies within the rest of this work are conducted using only the UCs for the reconstruction.
Comparing the performance of showers with θ_0 and θ_{45}, gave a first insight on what to expect of the core and energy estimations once showers of all incoming angles are reconstructed. It can be assumed that the results of the core and energy estimations of showers with a zenith angle between 0° and 45° lie somewhere between the results that are found here.

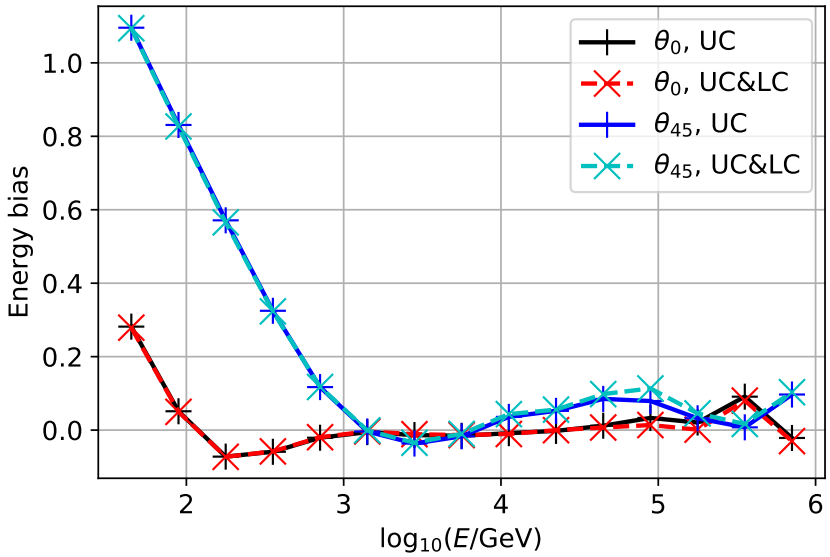

Figure 5.10: Energy bias for reconstructing showers with zenith angles θ_0 and θ_{45} for using only the UCs and using both cells together.

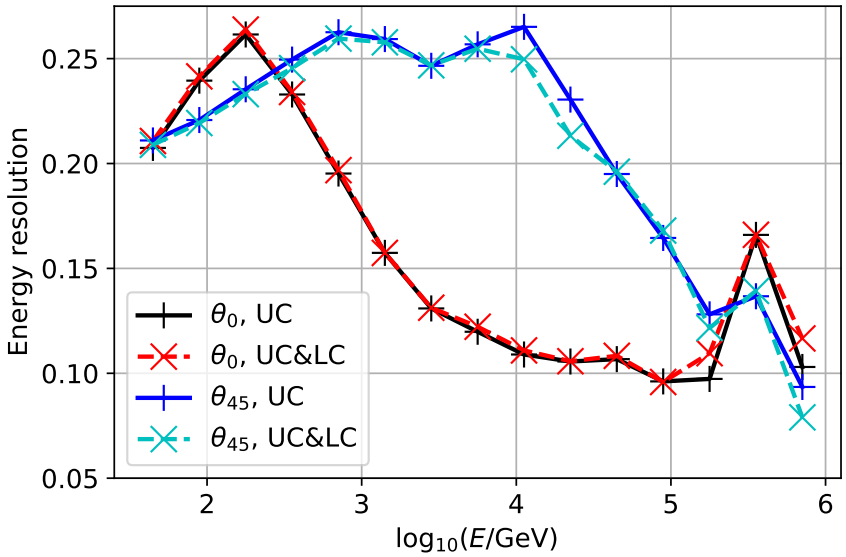

Figure 5.11: Energy resolution for reconstructing showers with zenith angles θ_0 and θ_{45} for using only the UCs and using both cells together.

5.3 Bin Optimisation

Up to this point, the binning used for the results in section 5.2 was picked by hand to get the chain running. In this section, the binning that is used for the templates of the test array is optimised. The parameters that will be optimised consist of the bin size of

the energy bins, $X_{\max}$ bins and the core bins that describe the distance r between the tank that measured a signal and the true shower core.
In the following, new sets of templates are created. For each set, the bin size of one of the parameters E, $X_{\max}$ and r is varied while the rest of the parameters are fixed to a specific bin size. This way, the influence of varying the bin size of specific parameters can be investigated individually. The simulations that are used for the optimisation are adjusted for optimising specific parameters to avoid making the simulations too computational intensive. In addition, the optimisation was conducted using only vertical showers which made the process independent of the zenith angle binning.

5.3.1 Core Bin Optimisation

The optimisation process starts by optimising the core bin size. The core bin describes the distance r between a tank that measured a signal and the true shower core and is used to bin the x-axis of each template (see figure 4.1a). The showers, which were simulated for the core bin optimisation, consisted of mono-energetic showers with an energy of 3 TeV and a maximum shower depth $X_{\max}$ between $150\,\mathrm{g/cm^2}$ and $750\,\mathrm{g/cm^2}$. The optimisation of the core bin size is independent of the energy binning due to the fact that only mono-energetic showers were used which means no specific size of the energy bin has to be set. The core bin size on the x-axis of the templates was varied for multiple sets of templates while the bin size of the maximum shower depth was fixed to $X_{\max} = 50\,\mathrm{g/cm^2}$.

The core bin optimisation is performed by evaluating the core resolution that can be acquired for reconstructing the simulated shower set with the different sets of templates. Similar to the core estimation in section 5.2, the first step to obtain the core resolution is to calculate the distance d between the reconstructed and the true shower core for all simulated events. Since only mono-energetic showers are used for the optimisation, the results can be shown in a 1D histogram. Figure 5.12 shows the distribution for a core bin size of 2 m. For each set of templates, and, thus, for each of the varying core bin sizes, such a 1D histogram size can be created. The core resolution is determined by the 68% containment radius of the distribution in figure 5.12 as it was defined in section 5.2.

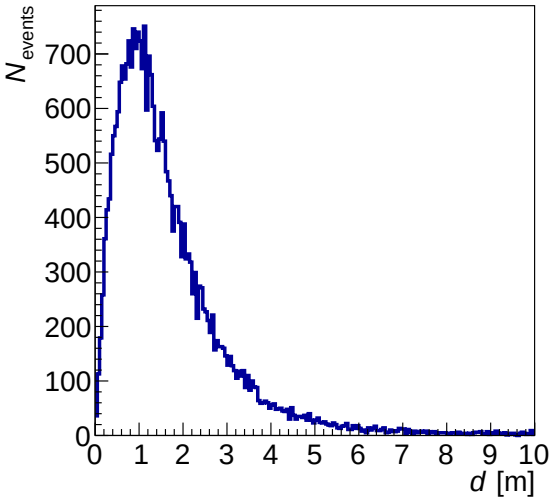

Figure 5.12: Distance d between the reconstructed and the true shower core for a core bin size of 2 m.

Figure 5.13 shows the results of the core resolution for multiple core bin sizes. One finds that the core resolution is improving for decreasing core bin sizes until the size of 2 m is reached. For a core bin size between 1 m and 2 m the resolution is equal. Decreasing the core bin size even more will lead to a rise of the core resolution.
If the bin size is too large, many measurements of N_{PE} are combined in the same core bin. This makes the reconstruction less precise which makes reaching a small core resolution impossible. Using too small bins will lead to overbinning. The binning is so small that artefacts in the core resolution start to dominate that do not actually describe any shower characteristics. This will increase the core resolution.
The optimal value for the core bin size was fixed at the bin size which would give the best possible result while also taking into account that the generation of the templates takes longer for smaller bin sizes and more statistics are necessary to fill the templates sufficiently if the bin size is small. For this reason, the optimal value for the core bin size was fixed at 2 m. At this point, the best core resolution can be obtained while the templates that are generated are also the least computational intensive.

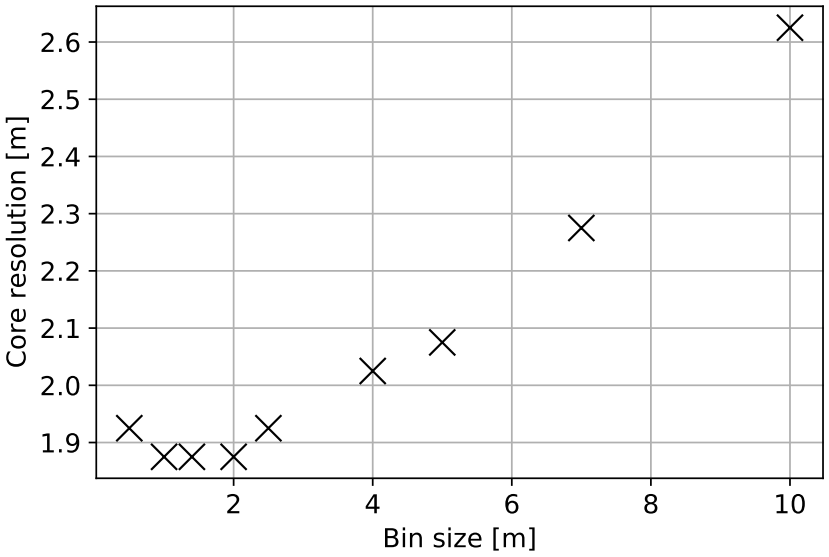

Figure 5.13: Core resolutions at different core bin sizes.

5.3.2 Energy Bin Optimisation

The next parameter that was optimised was the energy bin size. In this case, showers between 1 TeV and 7 TeV were simulated. The $X_{\max}$ of the showers was between 150 g/cm^2 and 750 g/cm^2. The $X_{\max}$ bin size was again set to 50 g/cm^2. For the core bin size, the optimal value that was determined in the core bin optimisation was used. The core bin size is therefore equal to 2 m. A set of templates is created for each varying energy bin size. To investigate the optimal energy bin size, the energy bias and energy resolution are evaluated. Like in the energy estimation in section 5.2, the difference between the reconstructed energy E_{reco} and the true energy E_{true} is calculated for each set of templates. In figure 5.14 the distribution is shown for an energy bin size of 0.05 in $\log_{10}(E/\text{GeV})$.

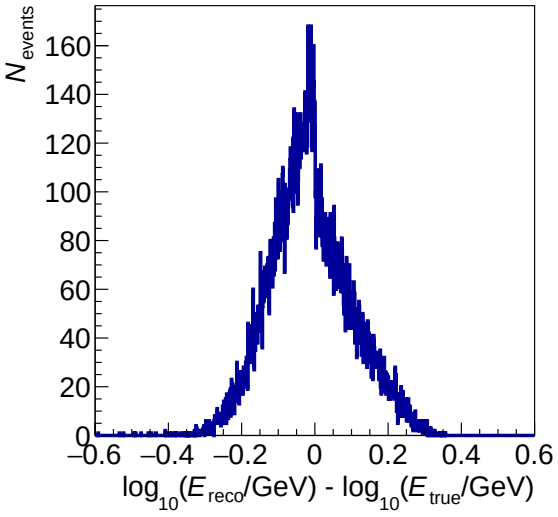

Figure 5.14: Difference between the true and reconstructed energy for an energy bin size of 0.05 in $\log_{10}(E/\text{GeV})$.

The energy bias is calculated as mean of the distribution in figure 5.14 while the resolution is calculated as the RMS of the distribution. The results of both the energy bias and the energy resolution at different energy bin sizes are shown in figures 5.15 and 5.16. Both energy bias and resolution worsen for increasing energy bin sizes. For energy bin sizes below 0.05, the results are approximately equal. The optimal energy bin size was therefore chosen as 0.05 in $\log_{10}(E/\text{GeV})$ to avoid a lot of computing time. The reason for why even smaller energy bin sizes than 0.025 were not tested was because the available statistics of the showers would not be sufficient enough to fill the templates at that point.

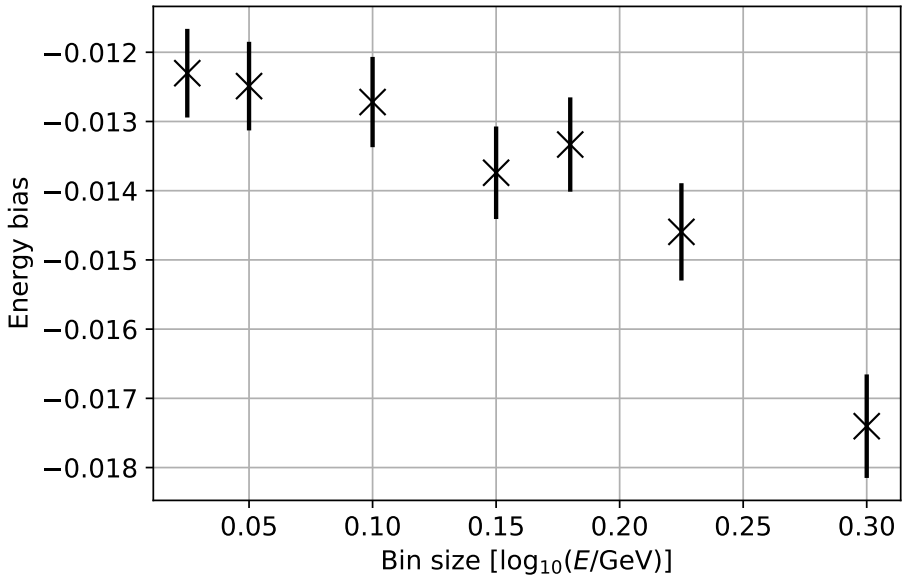

Figure 5.15: Energy bias at different energy bin sizes.

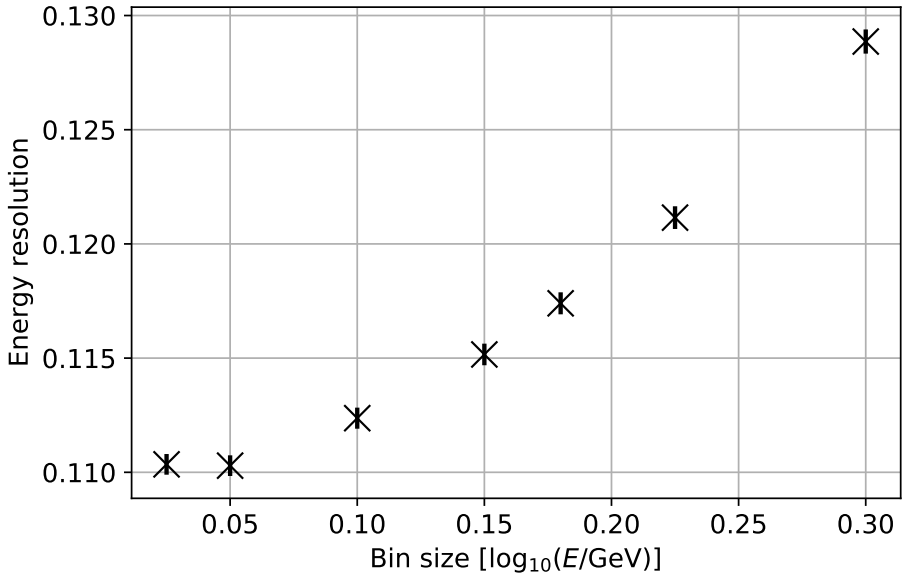

Figure 5.16: Energy resolution at different energy bin sizes.

5.3.3 $X_{\mathbf{max}}$ Bin Optimisation

Lastly, the $X_{\max}$ bin size was optimised. The bin sizes for the core and energy bins were taken from the previous optimisations with 2 m as the core bin size and 0.05 in $\log_{10}(E/\mathrm{GeV})$ as energy bin size. The $X_{\max}$ bin size was varied for each new set of templates. The showers that were used for the reconstruction were all mono-energetic showers with an energy of 3 TeV and the $X_{\max}$ was varying between 150 g/cm^2 and 750 g/cm^2.
To estimate the optimal $X_{\max}$ bin size, the difference between the true and the reconstructed $X_{\max}$ was calculated for all showers and for each $X_{\max}$ bin size. The resulting 1D distribution in figure 5.17 shows the results for a $X_{\max}$ bin size of 25 g/cm^2. Similar to the energy optimisation in section 5.3.2, a bias and resolution for the $X_{\max}$ can be determined. The $X_{\max}$ bias and $X_{\max}$ resolution for each $X_{\max}$ bin size are described by the mean and RMS of $X_{\max,\mathrm{reco}} - X_{\max,\mathrm{true}}$ in figure 5.17.

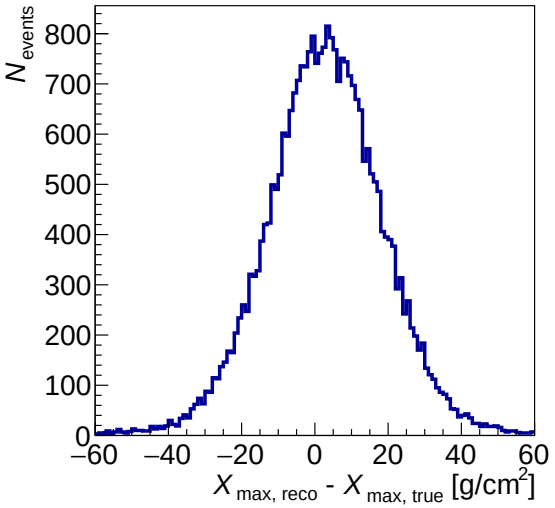

Figure 5.17: Difference between the true and reconstructed $X_{\max}$ at a $X_{\max}$ bin size of $25\,\mathrm{g/cm^2}$.

Figures 5.18 and 5.19 describe the $X_{\max}$ bias and resolution for varying $X_{\max}$ bin sizes. The optimal values for the bin size of $X_{\max}$ regarding the $X_{\max}$ bias and resolution can be found at a bin size of $25\,\mathrm{g/cm^2}$ and below. Like for the optimal energy bin size, the optimal $X_{\max}$ bin size is chosen to obtain the best possible results while making sure to keep the computation less intensive and allow the templates to be filled with enough statistics which leads to the optimal $X_{\max}$ bin size of $25\,\mathrm{g/cm^2}$.

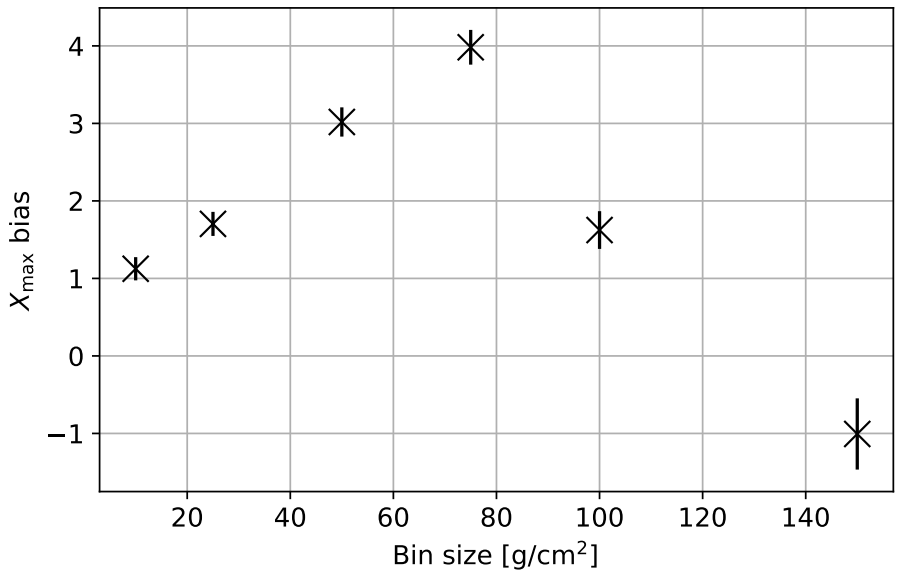

Figure 5.18: $X_{\max}$ bias at different $X_{\max}$ bin sizes.

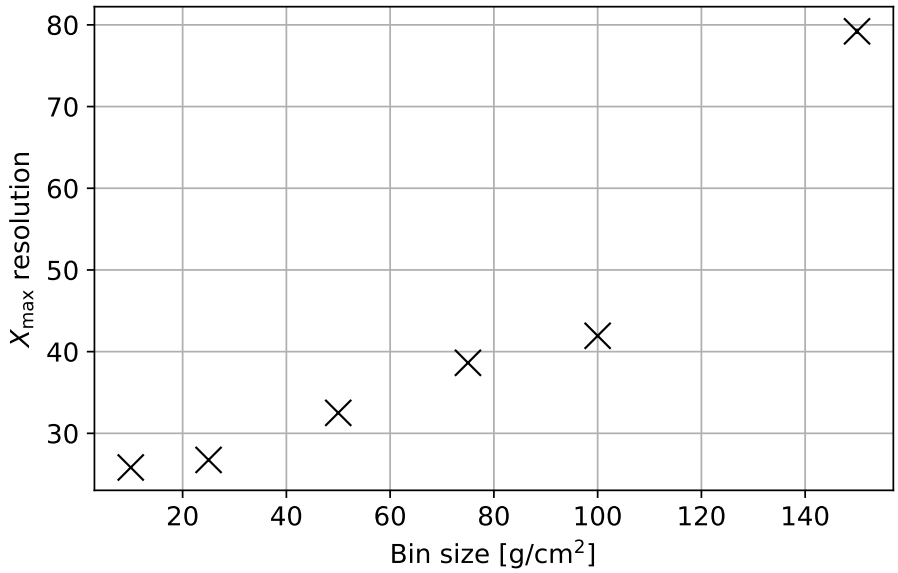

Figure 5.19: $X_{\max}$ resolution at different $X_{\max}$ bin sizes.

To summarise all results of section 5.3, the binning was optimised for the templates that are used to reconstruct showers with the test array described in section 5.1. The parameters that were optimised consisted of the energy, $X_{\max}$ and core bin sizes. The optimal values that were found are the core bin size of 2 m, the energy bin size of 0.05 in $\log_{10}(E/\mathrm{GeV})$ and the $X_{\max}$ bin size of 25 g/cm^2. At this point, it has to be mentioned that the optimisation performed in this section was only an optimisation of the templates at a certain point in the phase space, since the templates were only filled with vertical showers in a small energy range. Nevertheless, these results already give an insight on the bin optimisation for an array that follows the propositions for SWGO and can be used to speed up the bin optimisation once the final design of the SWGO array is determined.

Chapter 6

SWGO Reference Configuration

In this chapter, the information regarding the core and energy estimations of the test array will be used to perform a core and energy estimation for the reference layout of SWGO. In the following, this layout is described together with the design of the tanks and the binning that was used to create the templates for the reconstruction. Afterwards, the results of the core and energy estimations are shown.

6.1 Reference Configuration

The reference layout consists of a dense inner array with a radius of $r_\mathrm{i} = 160\,\mathrm{m}$ that is filled with 5719 tanks and a sparser outer array with the radius $r_\mathrm{o} = 300\,\mathrm{m}$ that is filled with 882 tanks. The tanks are placed in a hexagonal grid structure. The layout is shown in figure 6.1. The site is simulated at an observation height of 4700 m above sea level.
The geometry of the cylindrical, double-layered WCDs used in the array is described in table 6.1. One 8" PMT is placed in each cell. In the LC the PMT is fixed at the ceiling and in the UC it is fixed in the bottom of the cell.

Characteristics	Upper Cell	Lower Cell
radius [m]	1.91	1.91
height [m]	2.5	0.5
thickness [mm]	6.0	6.0
cover lining	polypropylene	tyvek
bottom lining	polypropylene	tyvek
wall lining	tyvek	tyvek

Table 6.1: Characteristics of the cylindrical, double-layered WCD tanks used in the reference configuration.

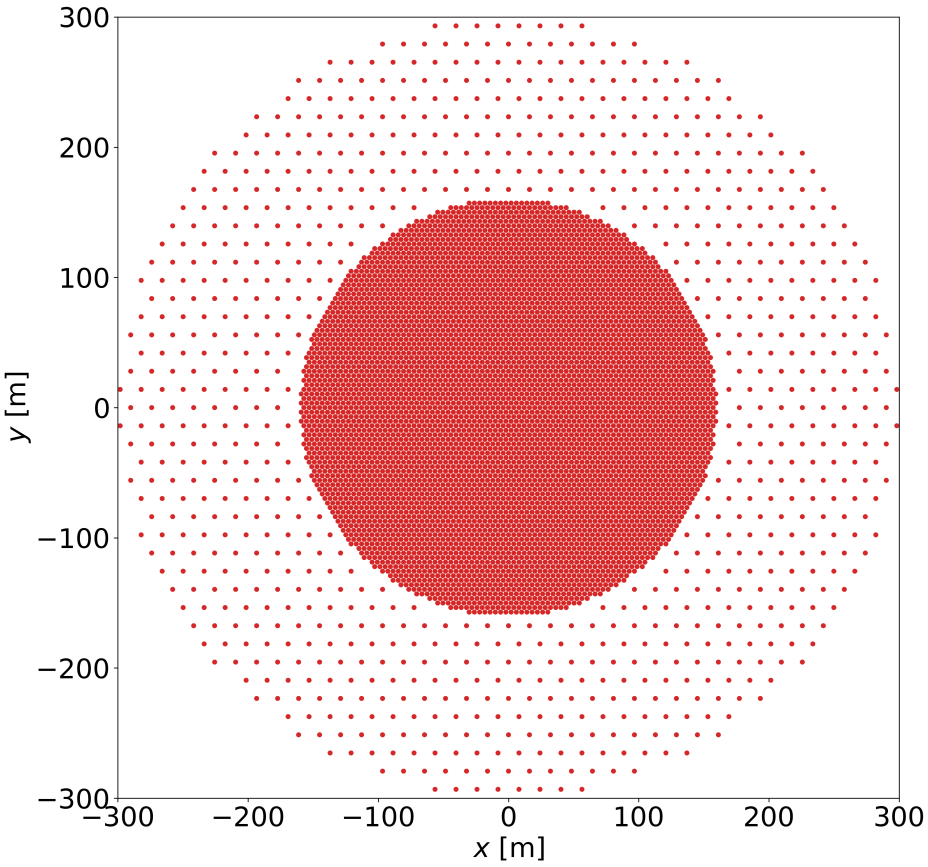

Figure 6.1: Layout of the reference configuration.

The binning for the templates can be found in table 6.2. The optimal binning that was obtained through the bin optimisation in section 5.3 was used for all parameters except for the X_{max} bin size which was set to $50\,\mathrm{g/cm^2}$ instead of the optimal value of $25\,\mathrm{g/cm^2}$ to make sure that the templates are filled sufficiently. Showers with an energy between 31.6 GeV and 1 PeV and a zenith angle of up to 50 ° were used to fill the templates.

Parameters	Range	Bin Size	Description
E	31.6 GeV to 1 PeV	0.05	binned in $\log_{10}(E/\mathrm{GeV})$
X_{max}	$150\,\mathrm{g/cm^2}$ to $750\,\mathrm{g/cm^2}$	$50\,\mathrm{g/cm^2}$	-
θ	0° to 50 °	0.06	binned in $\cos\theta$
r	0 m to 1000 m	2 m	-
$\log_{10}(N_{\mathrm{PE}})$	-4 to 8	0.1	binned in $\log_{10}(N_{\mathrm{PE}})$

Table 6.2: Binning of the energy E, zenith angle θ, maximum shower depth X_{max}, distance r of the tanks from the shower core and measured signal $\log_{10}(N_{\mathrm{PE}})$ of the templates that are used to reconstruct showers with the reference configuration.

6.2 Performance

In the following, core and energy estimations are conducted for the reference design. For this, showers with a zenith angle $\theta < 45\,^\circ$ were thrown on the inner array of the reference design. The trigger criterion for reconstructing a shower was tested for at least 25, 50 and 100 tanks triggered.

6.2.1 Core Estimation

The core estimation of the reference layout can be found in figure 6.2. Up to an energy of $\sim 3\,\text{TeV}$, the core resolution differs for the trigger criteria of 25, 50 and 100 tanks triggered. By increasing the threshold of triggered tanks at lower energies, showers with a low signal are sorted out which improves the reconstruction. After 3 TeV, the core resolution is equal for the different trigger criteria since most showers satisfy all three trigger criteria at these energies. At this point, the core resolution already lies below 10 m. Over all, the core resolution improves up to an energy of $\sim 100\,\text{TeV}$. At even higher energies, the core resolution could not be evaluated because of low statistics.

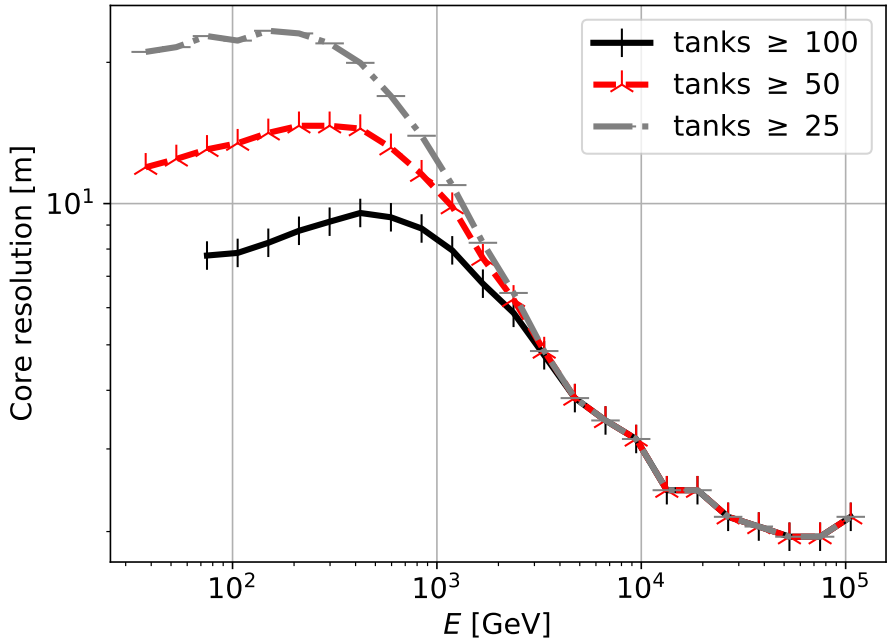

Figure 6.2: Core resolution of the reference layout for varying trigger criteria. The reconstructed showers with $\theta < 45\,^\circ$ were thrown on the inner array of the reference layout.

6.2.2 Energy Estimation

The energy bias and resolution of the reference layout is shown in figures 6.3 and 6.4. The results for varying trigger criteria are also compared to values that were calculated with HAWC [17] and a straw man design that was already evaluated for SWGO [4] to assess the quality of the energy estimation for the reference design. While results

similar to the straw man design are desired, it has to be taken into account that the straw man design is not an actually realised detector array but a toy design that was only used to estimate the possible performance of SWGO by scaling the performance of HAWC [4]. The straw man design shows significant differences to the reference design of SWGO which was based on the propositions made in chapter 3. Besides a different tank geometry, the straw man design is, for example, placed at a higher observation height of 5000 m. More information on the straw man design can be found in [4].

Similar to the core resolution, one can find that the energy bias and energy resolution of the reference design with the trigger criteria of at least 25, 50 and 100 tanks triggered only differ at energies below ~ 3 TeV.
Looking specifically at the energy bias in figure 6.3, one can find that the energy bias of the reference configuration aligns well with the one of HAWC and the straw man design. The results of the reference configuration resemble the results of the straw man design the most when a trigger criterion of at least 25 tanks triggered is used. For this trigger criterion, the stable region of the energy reconstruction starts at ~ 700 GeV when the energy bias starts to converge towards zero. Because of limited statistics, no reliable estimations on the energy bias at energies above 100 TeV could be made for the reference design.

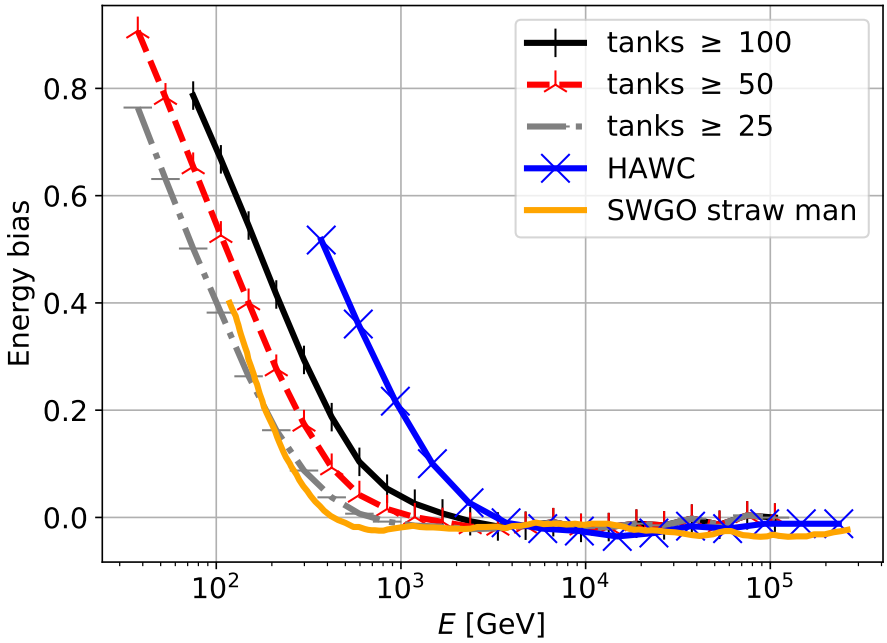

Figure 6.3: Energy bias of the reference layout for varying trigger criteria compared to results from HAWC [17] and the SWGO straw man design [4]. The reconstructed showers with $\theta < 45\,^\circ$ were thrown on the inner array of the reference layout.

The energy resolution (see figure 6.4) also agrees with the results that could be obtained with the straw man design, especially when the criterion of at least 25 tanks triggered is selected. While the value of the energy resolution of the reference design starts to rise above the one from the straw man design at energies in an order of 10 TeV, it is still

below the result of HAWC. Looking at the stable region for the energy reconstruction with the trigger criterion of at least 25 tanks triggered, one can see that the energy resolution improves from $\sim 65\,\%$ at energies around 1 TeV to $\sim 26\,\%$ at 100 TeV. Like for the energy bias, no investigations of the energy resolution could be conducted for energies above 100 TeV.

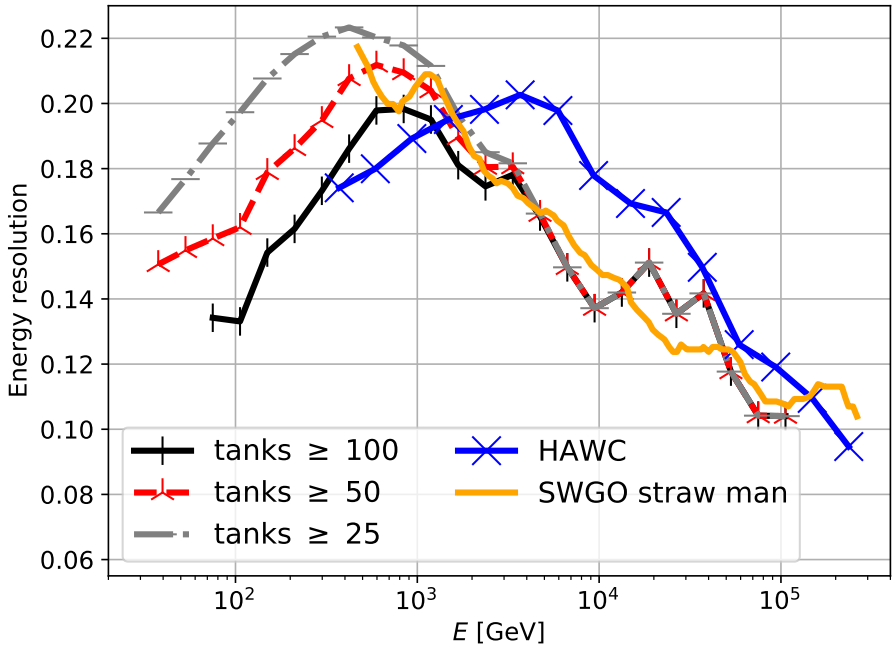

Figure 6.4: Energy resolution of the reference layout for varying trigger criteria compared to results from HAWC [17] and the SWGO straw man design [4]. The reconstructed showers with $\theta < 45\,^\circ$ were thrown on the inner array of the reference layout.

To summarise the results for the core and energy estimations of the reference layout, one can find that the results of the straw man design of SWGO could be well matched if a trigger criterion of at least 25 tanks triggered is applied. Adding statistics to fill the templates more at higher energies could potentially improve the results especially in regards to the energy resolution between 10 TeV and 100 TeV. In general, the reconstructions of showers with a primary energy of up to 100 TeV, that were conducted in the scope of this thesis while using the reference design of SWGO, show promising results, mostly aligning with the straw man design and even surpassing the results from HAWC.

Chapter 7

SWGO Super Configuration

Finally, the performance of the reconstruction is tested for the SWGO super configuration. The super configuration is intended to be a generalisation of the reference design described in section 6.1. Therefore, the dimensions of the super configuration exceed the ones specified in the propositions made for SWGO in chapter 3. First, the layout and the use of the super configuration is described. Afterwards, the results of the first performance tests regarding the shower reconstruction with various detector layouts, that were created with the super configuration, are given.

7.1 Layout of the Super Configuration

The array layout of the full super configuration can be found in figure 7.1. It is designed as an generalisation of the reference design of section 6.1. The tanks that are used for the super configuration are labelled as tanks A, B, C, D and R. They can be combined in various ways to create different array layouts. Comparing the performance of the various design options can give an insight on what detector layout combinations can be used for the future SWGO array.
Tanks that are labelled as R-tanks represent tanks that are also used in the reference layout described in section 6.1. A-tanks make up the very dense inner array that is marked in red in figure 7.1. In this inner array, which has a radius $r_{\mathrm{A}} \approx 170\,\mathrm{m}$, 6625 tanks are placed. Tanks B are used in the clusters of the super configuration. They are marked in grey in figure 7.1 and in figure 7.2 a zoom in on such a cluster can be found. Overall, 2970 tanks are used for the clusters. The large sparse outer array is made up by tanks C. They are marked in black in figure 7.1 and in the close up in figure 7.2. The sparse outer array spans from the end of the inner array to $r_{\mathrm{C}} = 565\,\mathrm{m}$ and has the same density as the outer array of the reference layout. Altogether, 4086 tanks are used to make up this part of the array. Tanks D are used to describe the denser outer array that lies between the end of the inner array and $r_{\mathrm{D}} = 350\,\mathrm{m}$. The dense outer array consists of 5334 tanks and is marked in blue in figures 7.1 and 7.2.

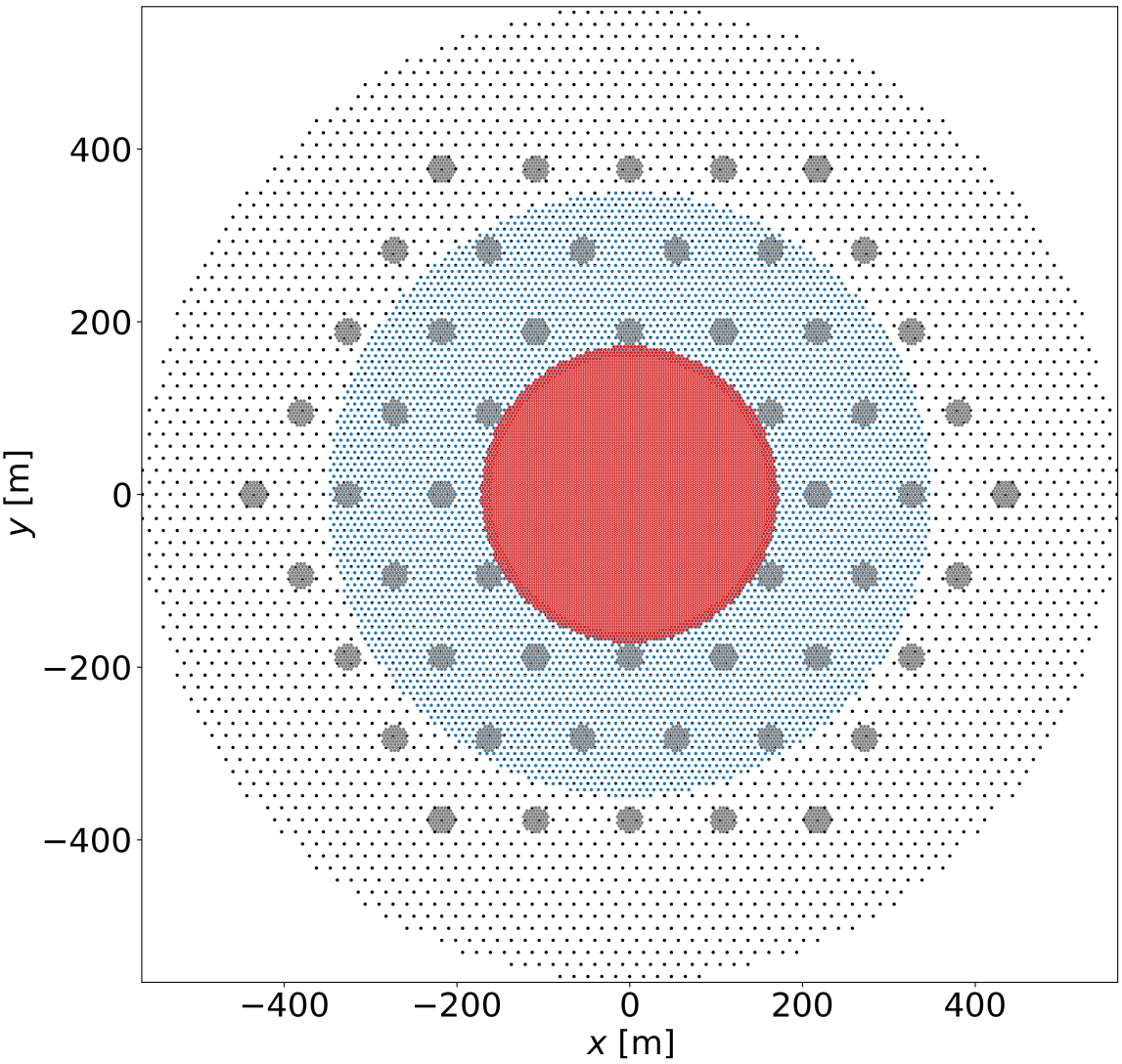

Figure 7.1: Layout of the super configuration. The red dots correspond to tanks A, the grey to tanks B, the black to tanks C and the blue to tanks D.

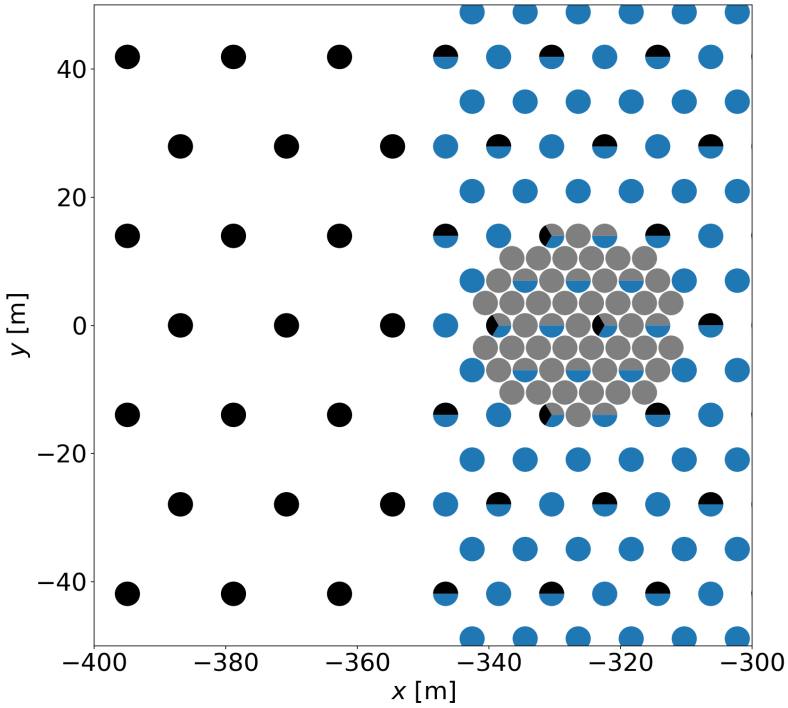

Figure 7.2: Zoom in on a cluster of the super configuration. The grey dots correspond to tanks B, the black to tanks C and the blue to tanks D.

Apart from their label that describes how the tanks can be used for varying layout designs, the tanks do not differ from each other in their geometry. For the tanks, cylindrical, double-layered WCDs are used. One 10" PMT was placed in each cell. The PMT in the LC was placed on the ceiling of the cell and the PMT in the UC was placed on the bottom of the cell. The geometry of the tanks is described in table 7.1.

Characteristics	Upper Cell	Lower Cell
radius [m]	1.91	1.91
height [m]	2.5	0.5
thickness [mm]	6.0	6.0
cover lining	polypropylene	tyvek
bottom lining	polypropylene	tyvek
wall lining	tyvek	tyvek

Table 7.1: Description of the cylindrical, double-layered WCD tanks used in the super configuration.

The general location of the site is set at an observation height of 4700 m. The Monte Carlo showers, which were used to generate the templates, had energies between 31.6 GeV and 1 PeV and a zenith angle of up to 50 °. The binning that was used for the templates can be found in table 7.2. The bin size of the energy and $X_{\max}$ was bigger than the optimal values that were determined in section 5.3. Because of the huge size of the

super configuration, the shower simulations are very computational intensive. Only few showers were simulated so far to get a first estimation on the performance of the super configuration. With a smaller binning than what was chosen in table 7.2, the templates could not have been filled sufficiently.

Parameters	Range	Bin Size	Description
E	31.6 GeV to 1 PeV	0.3	binned in $\log_{10}(E/\mathrm{GeV})$
X_{max}	150 g/cm^2 to 750 g/cm^2	150 g/cm^2	-
θ	0° to 50 °	0.06	binned in cosθ
r	0 m to 1300 m	2m	-
$\log_{10}(N_{\mathrm{PE}})$	-4 to 8	0.1	binned in $\log_{10}(N_{\mathrm{PE}})$

Table 7.2: Binning of the energy E, zenith angle θ, maximum shower depth X_{max}, distance r of the tanks from the shower core and measured signal $\log_{10}(N_{\mathrm{PE}})$ of the templates that are used to reconstruct showers with the super configuration.

7.2 First Performance Tests

Since the super configuration is supposed to be a generalisation of the reference configuration, first performance tests were conducted for combinations of the reference layout with additional tanks B, C and D. All array layouts that were used in the following, can be found in figures 8.1-8.7 in the appendix.
The trigger criterion for the number of tanks that had to be triggered to start the reconstruction was set to 25 or more, since this threshold gave comparable results to the performance of the straw man design of SWGO [4] for core and energy estimations of the reference layout in section 6.2. The showers that were reconstructed were thrown within a 300 m radius of the array centre which is equal to the radius of the reference design. Because of the limited statistics, only showers with a zenith angle of up to $\theta = 35\,^\circ$ and energies of up to the order of 100 TeV are reconstructed in the following.

7.2.1 Core Estimation

Figure 7.3 shows the results of the core estimation of various array layouts. One can see that the core resolution for the reference layout (orange) is very high throughout all energy ranges and never goes below 10 m. This is a worse result than what could be accomplished with the reference layout in section 6.2.1. The reason for this is that, previously, only showers that were thrown on the inner array, and thus within a radius of 160 m of the array centre, were used for the calculation of the core resolution. Here, showers that hit the edge of the array are also included in the reconstruction. If a shower hits the edge of the array, the number of tanks that measured a signal is much smaller than the one that could be measured if a shower hits the centre of the array. In the reconstruction, it is therefore harder to fit these showers to their correct templates which, in turn, results in a worse core resolution. In addition, because of the limited statistics, larger bin sizes that were not optimised yet had to be chosen and the templates could not be filled as much. This also influences the results negatively.

Looking at the core resolutions of the combined layouts in figure 7.3, one can find that, at first, the core resolution improves with increasing energies for all combinations of the tanks B, C and D with the reference design. After energies of around 100 TeV, the core resolution seems to worsen again for most of the different designs. This is most likely caused by the limited statistics that were used to generate the templates and the limited number of showers that were reconstructed with these layouts.
Comparing the results of the core resolution of the combined layouts with each other shows that, in general, the core resolution improves when more tanks are added to the area on which the showers are thrown. Using all additional tanks B, C and D will give the best results for the core resolution.

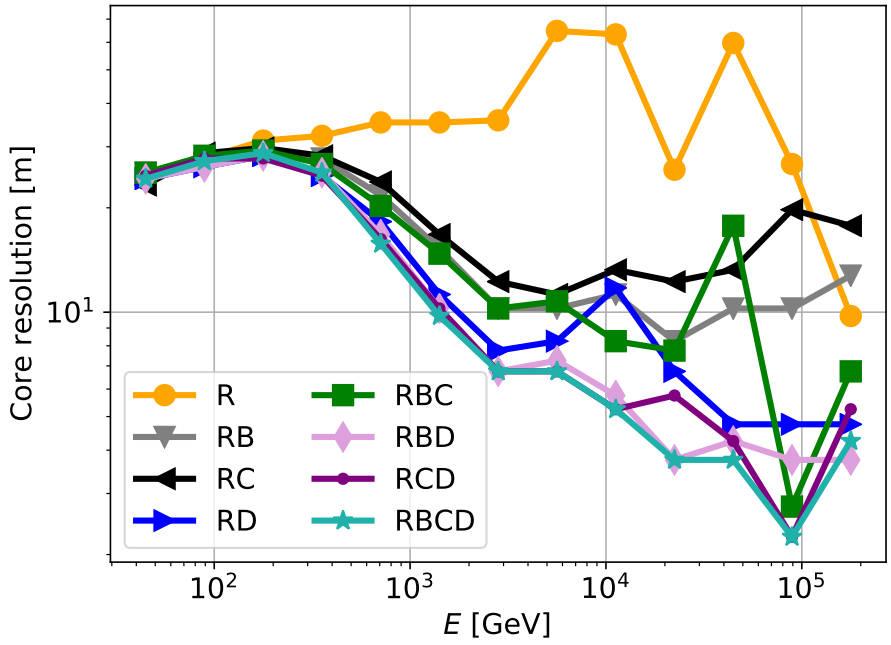

Figure 7.3: Core resolution of different array layouts (see figures 8.1-8.7) that were created by combining the tanks R of the reference layout with tanks B, C and D. At least 25 tanks had to be triggered for the reconstruction. All reconstructed showers were thrown within a 300 m radius from the array centre and had a zenith angle $\theta < 35\,°$.

7.2.2 Energy Estimation

Figures 7.4 and 7.5 show the results for the energy bias and energy resolution of the different layouts that were created with the super configuration compared to the results that were obtained with HAWC [17] and the straw man design that was evaluated for SWGO [4]. Since the layout of HAWC, the straw man design of SWGO and the super configuration, that is presented here, are greatly different when it comes to the size of the arrays and the geometry and distribution of the tanks, the results from HAWC and the straw man design will only operate as guidance to estimate the first performance of the super configuration.
Using only the reference design leads to a worse result of the energy reconstruction than what could be measured with the reference configuration in section 6.2.2. Once

again, the effect of the showers that are thrown on the edge of the array is most likely contributing to this. The energy bias and resolution of the different layouts improve as more tanks are added to the array. The best results can again be archived by using all tanks B, C and D with the reference design.
Comparing the energy bias of the super configuration with HAWC and the SWGO straw man design, it can be seen that the results of the combined layouts are relatively similar to the energy bias of the straw man design up to an energy in the order of 100 TeV and similar to HAWC between ~ 3 TeV and ~ 100 TeV. After ~ 100 TeV the results seem to worsen which is, similar to the core resolution, most likely caused by less filled templates and a smaller number of reconstructed showers.

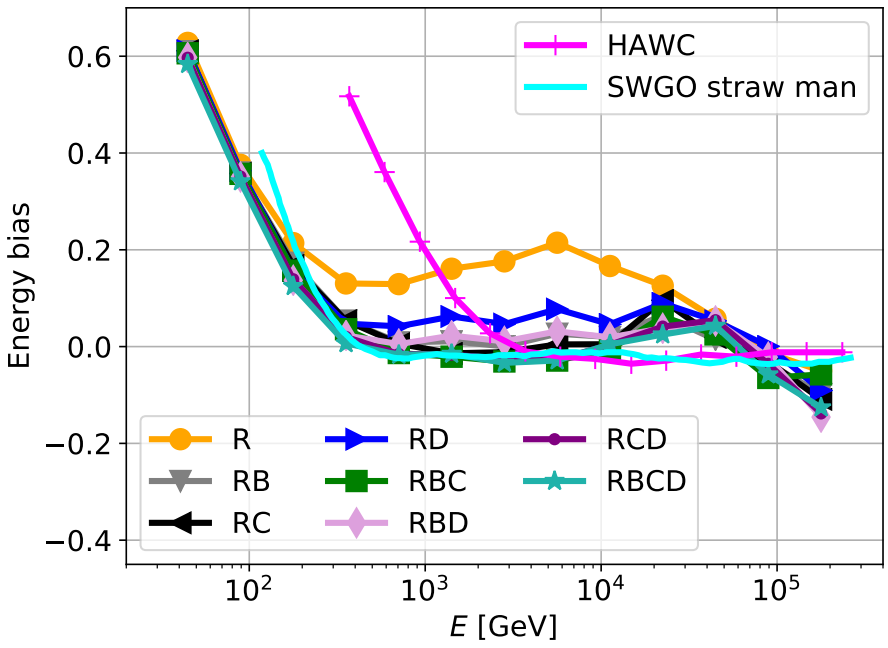

Figure 7.4: Energy bias of different array layouts (see figures 8.1-8.7) created by combining tanks R of the reference layout with tanks B, C and D. At least 25 tanks had to be triggered for the reconstruction. All reconstructed showers were thrown within a 300 m radius from the array centre and had a zenith angle $\theta < 35\,°$. The results were compared to HAWC [17] and the straw man design created for SWGO [4].

In case of the energy resolution, only the layouts that use the tanks RC, RBC, RCD and RBCD can reach similar results to HAWC and the straw man design of SWGO. The energy at which this overlap can be found is very small. It is only the case for energies in the order of ~ 1 TeV. The reason for the high deviation from the results of HAWC and the straw man design in the energy resolution can most likely be attributed to the limited number of showers that are available for the super configuration.

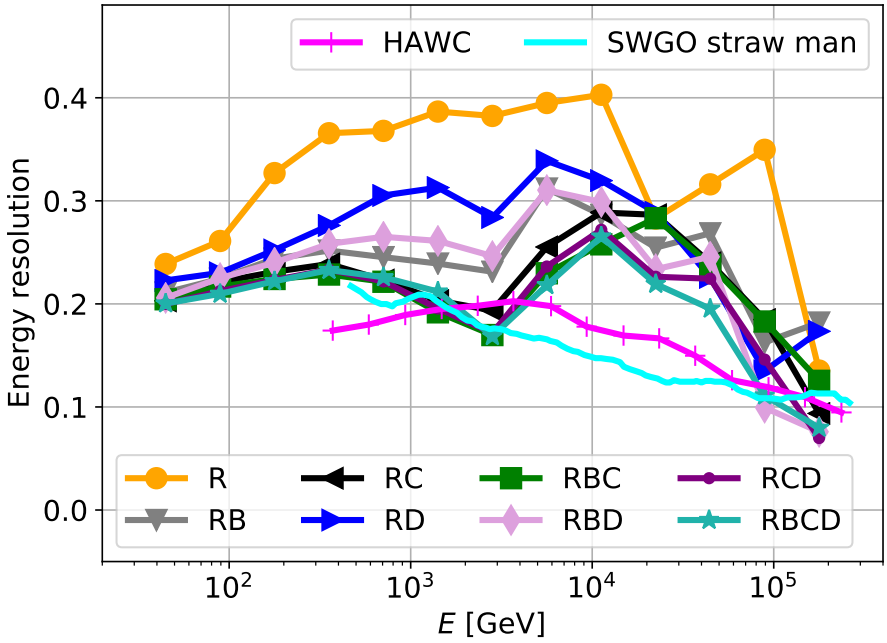

Figure 7.5: Energy resolution of different array layouts (see figures 8.1-8.7) created by combining tanks R of the reference layout with tanks B, C and D. At least 25 tanks had to be triggered for the reconstruction. All reconstructed showers were thrown within a 300 m radius from the array centre and had a zenith angle $\theta < 35\,°$. The results were compared to HAWC [17] and the straw man design created for SWGO [4].

Summarising the first results of the core and energy estimations of the different layouts of the super configuration, one can find that the shower reconstruction for the super configuration layouts still has to be improved before concrete statements can be made about the performance of the individual array layouts. In general, a higher amount of statistics is necessary since a lot of templates, that were created for the super configuration, are still insufficiently filled, even though a larger bin size was already set. The sparsely filled templates will affect the whole reconstruction negatively.
Nevertheless, it could be shown that the template-based reconstruction method can also be applied for different layouts of the super configuration. In addition, a first insight on the performance of different layouts, that can be created by combining the reference design with additional clusters (tanks B), a sparse outer array (tanks C) and a dense outer array (tanks D), could be given. So far, it seems like the performance of the reconstruction improves if the number of tanks in the area where the showers are thrown increases. A fixed rule about which tank type gives the best results can not be reliably defined so far because of the limited statistics. Once more simulations are available, the core and energy estimations can be repeated for the designs that were introduced here.

Chapter 8

Summary and Outlook

In this thesis, core and energy estimations for reconstructing gamma-ray induced EASs were performed for SWGO. For this purpose, at first, a test layout was designed which was modelled after propositions set by SWGO [14]. It uses cylindrical, double-layered WCDs with one PMT in each cell and consists of a densely packed inner array and a sparser filled outer array. At first, core and energy estimations were performed for vertical showers only. The performance of the reconstruction while using only the UCs of the tanks was compared with the performance while reconstructing showers with both the UCs and the LCs of the tanks. This was later repeated for showers that had an incoming zenith angle of $\theta = 45°$.
Comparing the performance of reconstructing vertical showers and showers with $\theta = 45°$ gave a first insight on how much the reconstruction of more inclined showers influences both the core and the energy estimations.
It was found that the additional use of the LCs for the reconstruction was neither improving nor worsening the results of the core and energy estimations for vertical showers and showers with $\theta = 45°$. This was attributed to the fact that the saturation of the PMTs in the WCD cells is not yet taken into account in the simulations.

Using the information gathered from the test array, the performance regarding core and energy reconstructions with the SWGO reference configuration was evaluated. For this, simulated showers with a zenith angle θ of up to 45° were used. To have some measure of value for the performance of the core and energy reconstructions that were conducted with the reference design, the results were compared to the results from HAWC [17] and the straw man design that was created for SWGO [4].
It was shown that the core and energy estimations that could be obtained for the reference configuration were agreeing well with both HAWC and the straw man design, especially when a trigger criterium of at least 25 tanks triggered was set. At energies above of $\sim 100\,\mathrm{TeV}$ no further investigations could be made because of limited statistics.

Lastly, different extensions of the reference configuration were created with the help of the SWGO super configuration. In general, the super configuration consists of a very dense inner array, multiple tank clusters, a big sparse outer array and a smaller dense outer array. These array components were used together with the reference configuration to create seven different array layout designs. In the end, the core and

energy estimations for each layout were compared to the results from HAWC [17] and the SWGO straw man design [4]. Since the super configuration simulations were very limited in statistics, the performance of the different layouts was only seen as preliminary and no reliable measure on which exact tanks give the best results when combined with the reference configuration could be found so far. Nevertheless, an improvement of the performance could be observed for array layouts with an increasing number of tanks.

The next step regarding future core and energy estimations for SWGO will include increasing the number of statistics for gamma-ray induced showers with energies in the order of 100 TeV and higher, for the reference configuration, as well as increasing the number of simulations as a whole when it comes to the super configuration.
Further optimisations of the fitting procedure and the smoothing procedure of the templates are planned. An optimisation regarding the bin sizes of the templates of the reference configuration can also be undertaken.
A saturation threshold of the PMTs will be implemented in the module to imitate the expected saturation of the PMTs in real data. As soon as this is done, it can be reassessed how the reconstruction with the additional LCs influences the performance.
In addition, a goodness of fit of the reconstructed showers will be implemented in the near future. This goodness of fit can be used as gamma-hadron separator to distinguish hadron-induced EASs from gamma-ray induced ones [18]. Together with the other gamma-hadron separators that are being developed for SWGO, this goodness of fit will help to further improve the hadron-like background rejection capabilities of SWGO.

Appendix

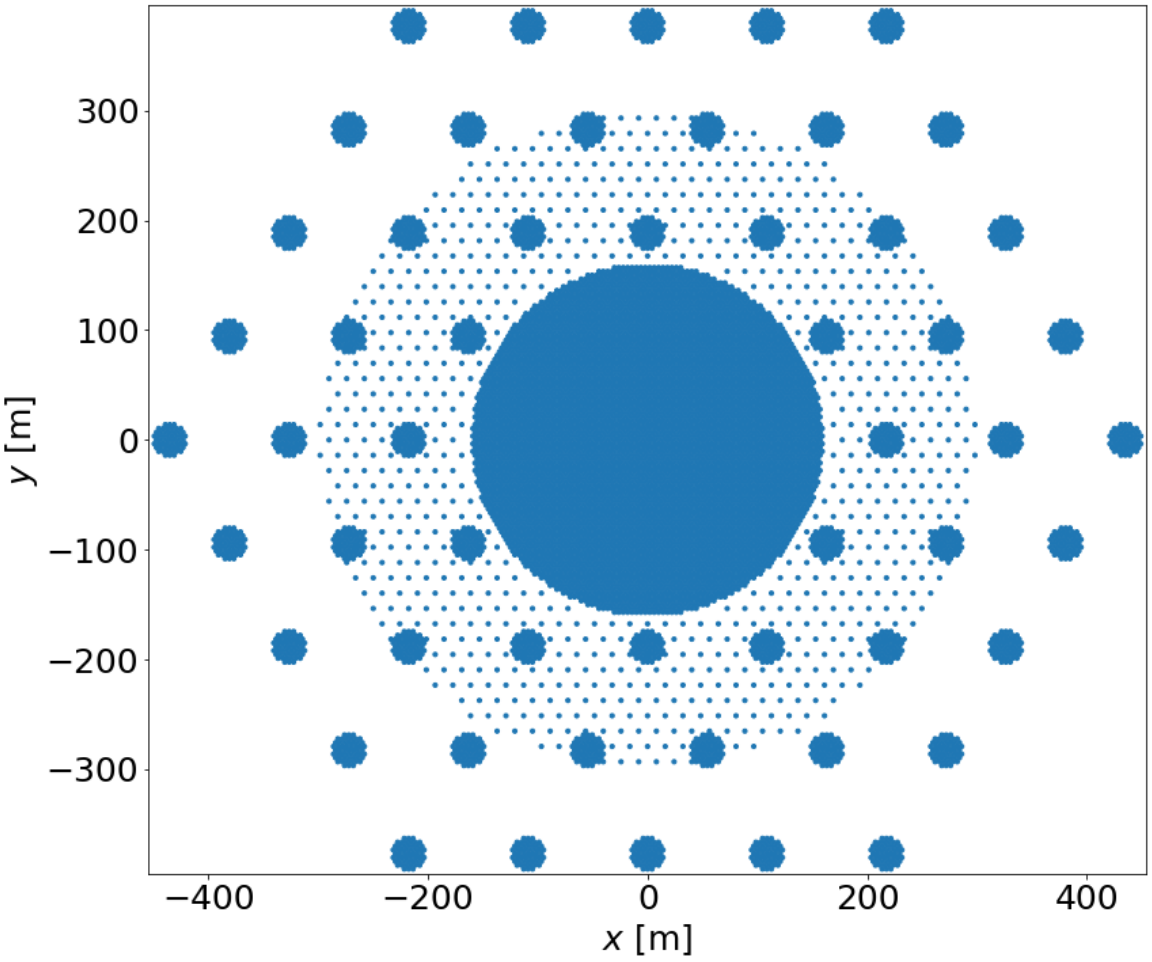

Figure 8.1: Reference layout combined with tanks B.

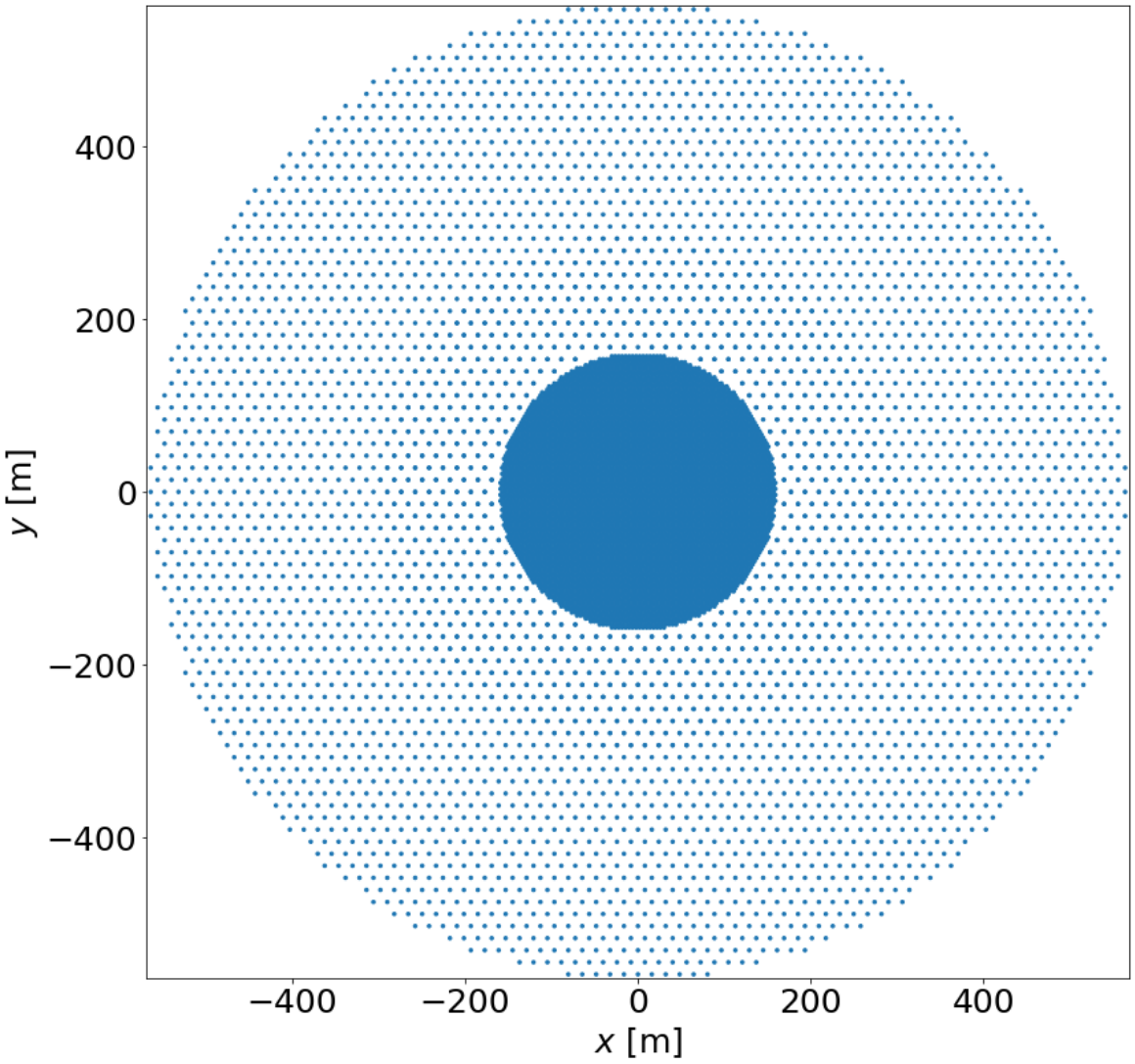

Figure 8.2: Reference layout combined with tanks C.

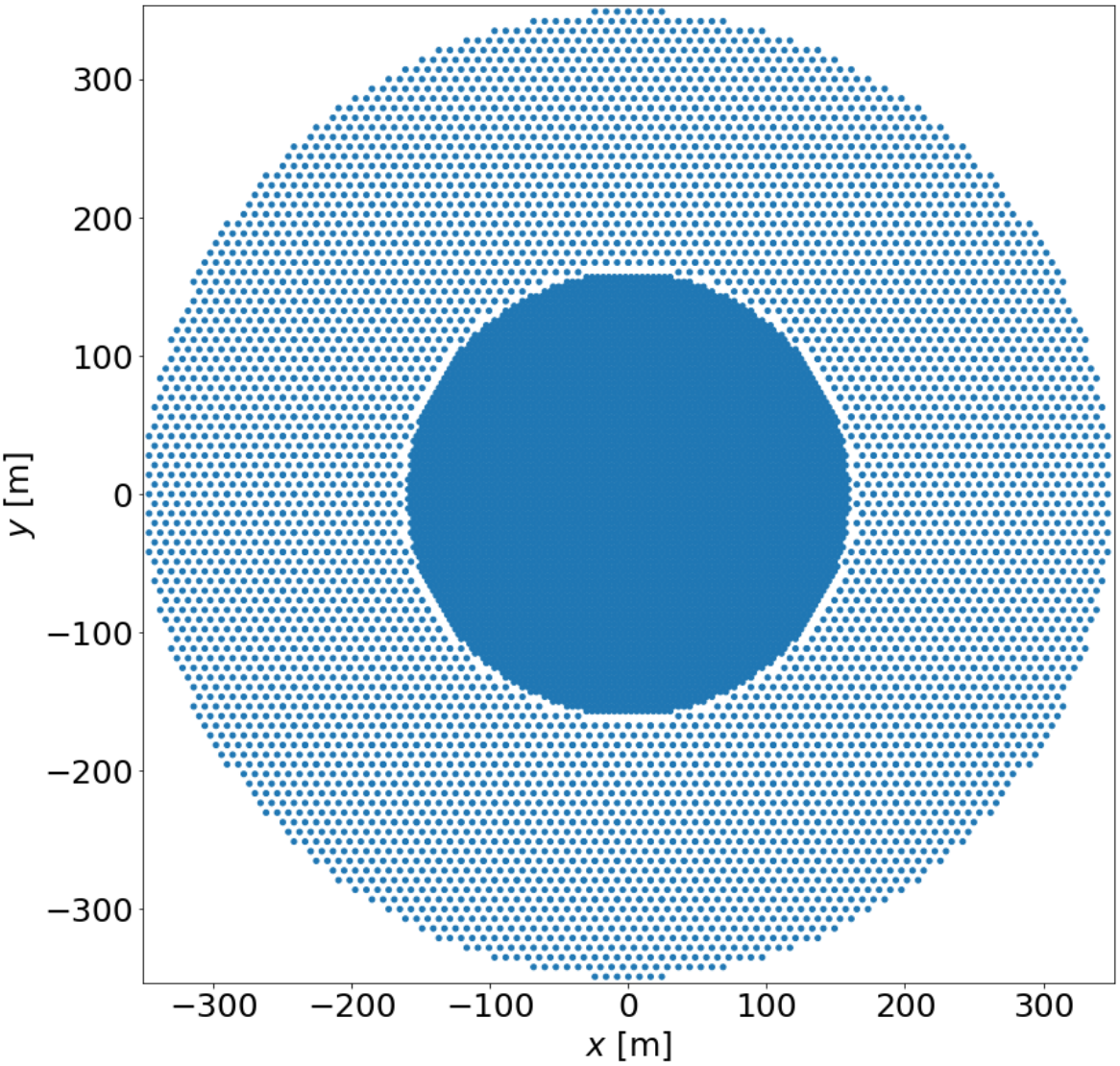

Figure 8.3: Reference layout combined with tanks D.

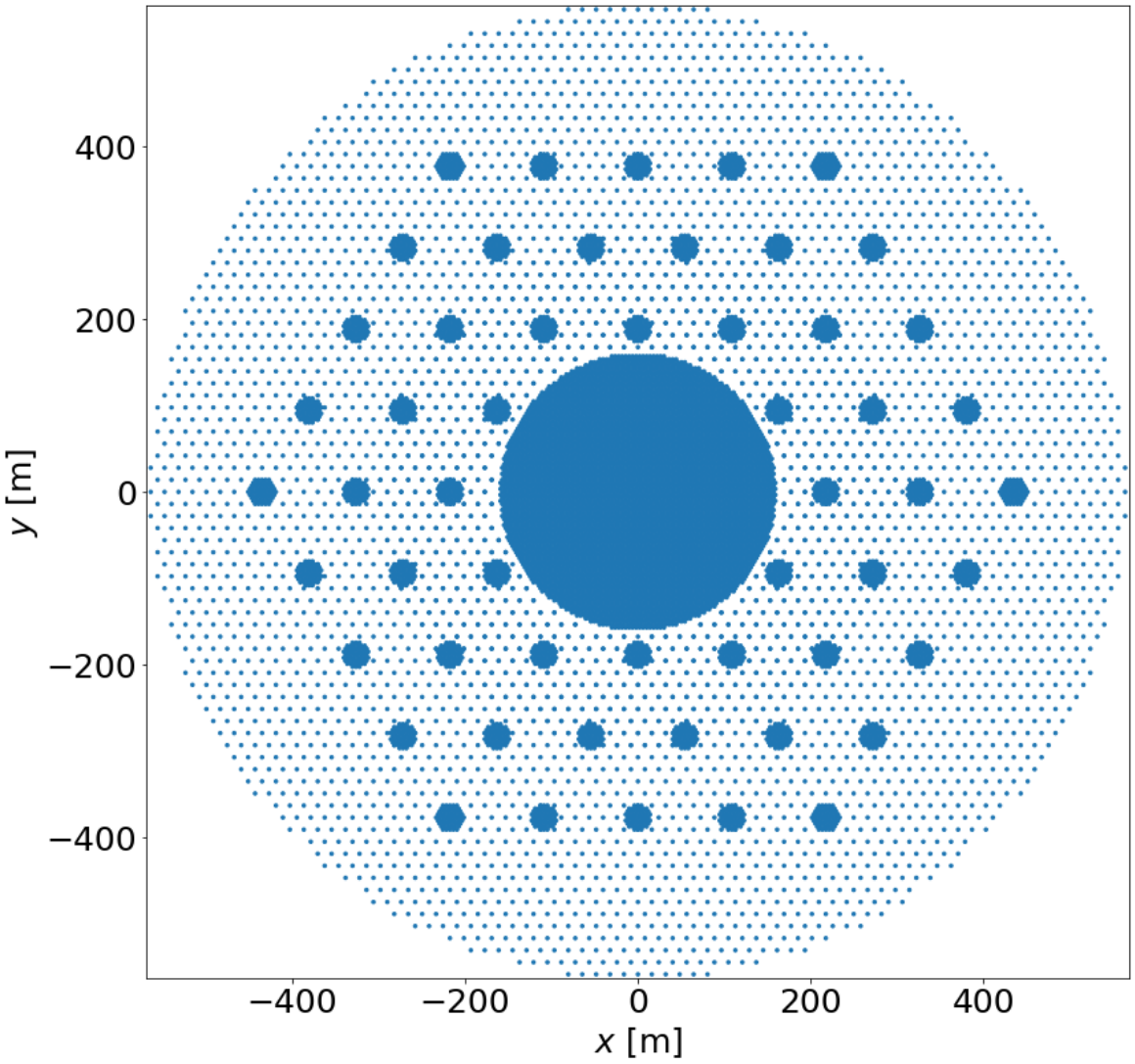

Figure 8.4: Reference layout combined with tanks B and C.

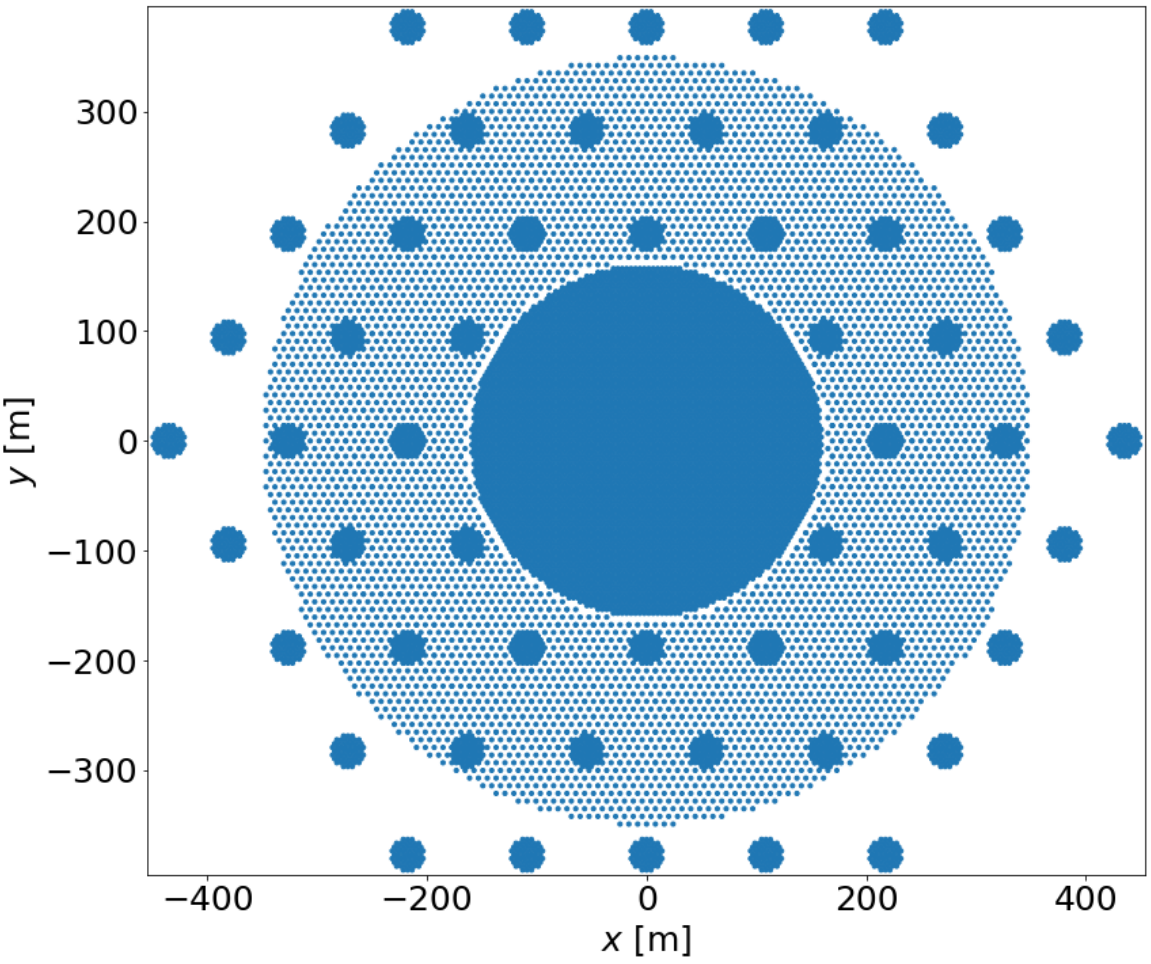

Figure 8.5: Reference layout combined with tanks B and D.

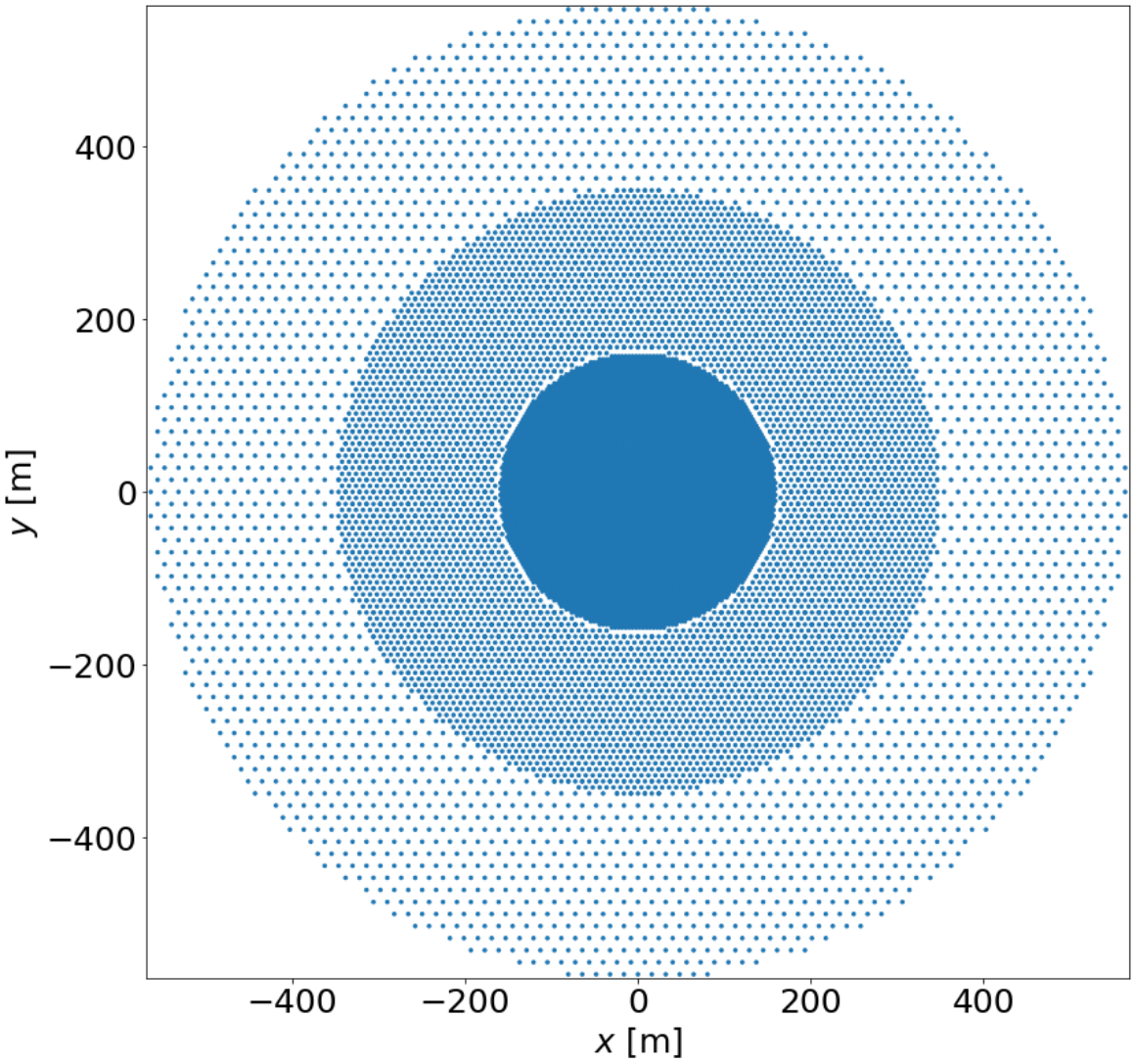

Figure 8.6: Reference layout combined with tanks C and D.

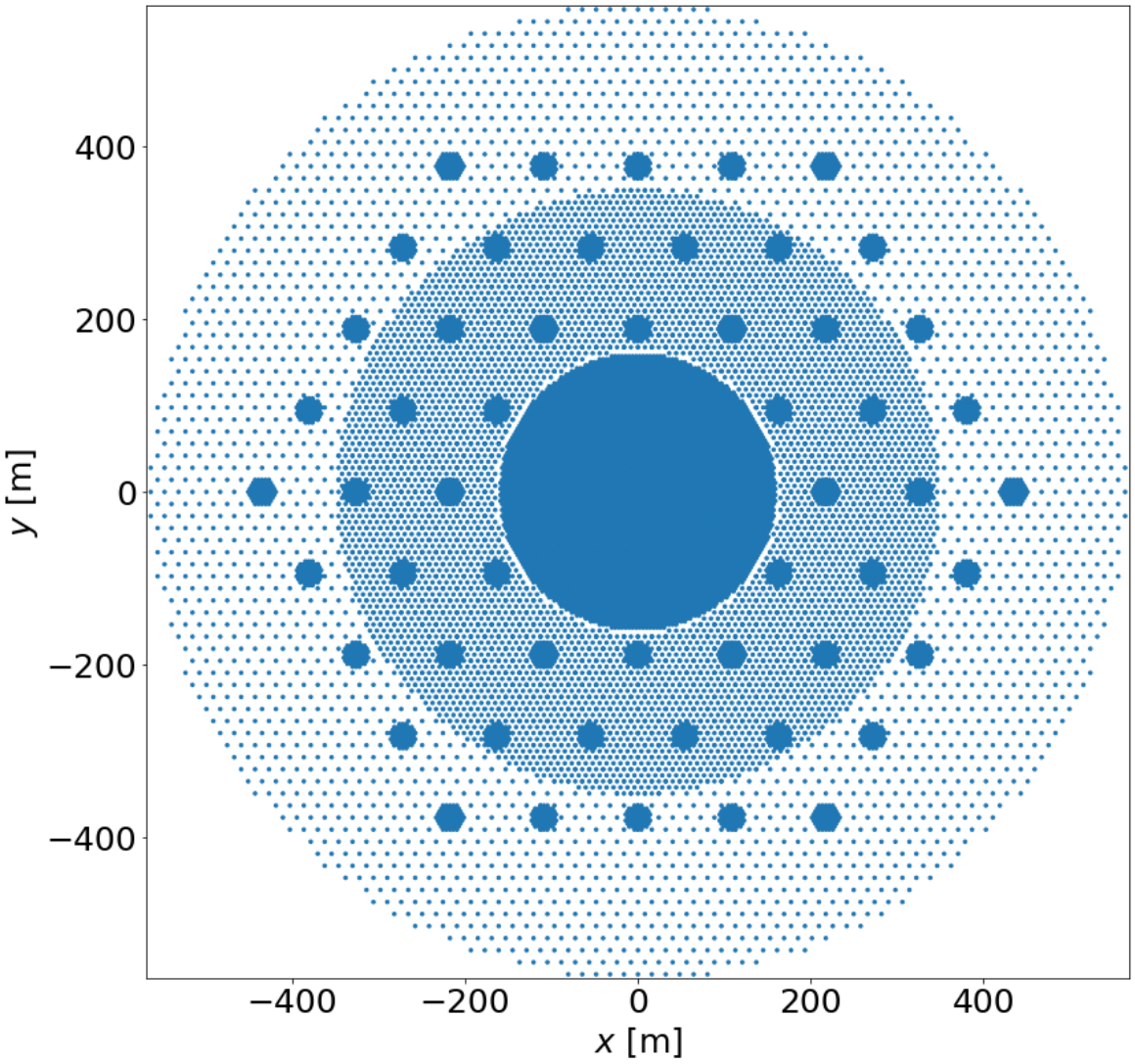

Figure 8.7: Reference layout combined with tanks B, C and D.

References

[1] Abeysekara, A.U. et al. (2017): Observation of the Crab Nebula with the HAWC Gamma-Ray Observatory. *arXiv e-prints*. arXiv: https://arxiv.org/abs/1701.01778

[2] Acharya, B.S. et al. (2018): Science with the Cherenkov Telescope Array. *arXiv e-prints*. arXiv: https://arxiv.org/abs/1709.07997

[3] Agostinelli, S. et al. (2003). Geant4 - a simulation toolkit. *Nuclear Instruments and Methods in Physics Research Section A: Accelerators, Spectrometers, Detectors and Associated Equipment*. 506. 250-303, DOI: https://doi.org/10.1016/S0168-9002(03)01368-8

[4] Albert, A. et al. (2019). Science Case for a Wide Field-of-View Very-High-Energy Gamma-Ray Observatory in the Southern Hemisphere. *arXiv e-prints*. arXiv: https://arxiv.org/abs/1902.08429

[5] Atwood, W.B. et al. (2009). THE LARGE AREA TELESCOPE ON THE *FERMI GAMMA-RAY SPACE TELESCOPE* MISSION. *The Astrophysical Journal*. 697. 1071–1102, DOI: https://doi.org/10.1088/0004-637x/697/2/1071

[6] Bai, X. et al. (2019). The Large High Altitude Air Shower Observatory (LHAASO) Science White Paper. *arXiv e-prints*. arXiv: https://arxiv.org/abs/1905.02773

[7] Cortina, J. (2005). Status and First Results of the MAGIC Telescope. *Astrophysics and Space Science*. 297. 245-255. DOI: https://doi.org/10.1007/s10509-005-7627-5

[8] Greisen, K. (1966). End to the Cosmic-Ray Spectrum?. *Physical Review Letters*. 16. 748-750. DOI: https://doi.org/10.1103/PhysRevLett.16.748

[9] Salesa Greus, F. (2016). First Results from the HAWC Gamma-Ray Observatory. *Nuclear and Particle Physics Proceedings*. 273–275. 289–294, https://doi.org/10.1016/j.nuclphysbps.2015.09.040

[10] Grupen, C. (2020). *Astroparticle Physics*. 2. Springer. DOI: https://doi.org/10.1007/978-3-030-27339-2

[11] Heck, D. et al. (1998). CORSIKA: A Monte Carlo Code to Simulate Extensive Air Showers. FZKA 6019

[12] Hess, V. (1912). Durchdringende Strahlung bei sieben Freiballonfahrten. *Physikalische Zeitschrift*. 13. 1084-1091.

[13] Hinton, J.A. (2004). The Status of the H.E.S.S. Project. *New Astronomy Reviews*. 48. 331-337. arXiv: https://arxiv.org/abs/astro-ph/0403052

[14] Huentemeyer, P. et al. (2019). The Southern Wide-Field Gamma-Ray Observatory (SWGO): A Next-Generation Ground-Based Survey Instrument for VHE Gamma-Ray Astronomy. *arXiv e-prints*. arXiv: https://arxiv.org/abs/1907.07737

[15] Holder, J. et al. (2006). The First VERITAS Telescope. *Astroparticle Physics*. 25. 391-401. arXiv: https://arxiv.org/abs/astro-ph/0604119

[16] James, F. Roos, M. (1975). Minuit - a system for function minimization and analysis of the parameter errors and correlations. *Computer Physics Communications*. 10. 343—367. DOI: https://doi.org/10.1016/0010-4655(75)90039-9

[17] Joshi, V. et al. (2019). A Template-based γ-ray Reconstruction Method for Air Shower Arrays. *arXiv e-prints*. arXiv: https://arxiv.org/abs/1809.07227

[18] Joshi, V. (2019). *Reconstruction and Analysis of Highest Energy γ-Rays and its Application to Pulsar Wind Nebulae*. DOI: https://doi.org/10.11588/heidok.00026062

[19] Matthews, J. (2005). A Heitler model of extensive air showers. *Astroparticle Physics*. 22. 387–397. DOI: https://doi.org/10.1016/j.astropartphys.2004.09.003

[20] Schoorlemmer, H. (2019). A next-generation ground-based wide field-of-view gamma-ray observatory in the southern hemisphere. *Proceedings of Science*. ICRC2019. 785. DOI: https://doi.org/10.22323/1.358.0785

[21] Zyla, P.A. et al. (2020). Review of Particle Physics. *Progress of Theoretical and Experimental Physics*. 2020. 083C01 . DOI: https://doi.org/10.1093/ptep/ptaa104

Acronyms

COM centre of mass

CTA Cherenkov Telescope Array

CORSIKA COsmic Ray SImulations for KAscade

EAS Extensive Air Shower

Fermi-LAT Large Area Telescope

GZK Greisen-Zatsepin-Kuzmin

HAWC High-Altitude Water Cherenkov

H.E.S.S. High Energy Stereoscopic System

IACT Imaging Atmospheric Cherenkov Telescope

LHAASO Large High Altitude Air Shower Observatory

LDF Lateral Distribution Function

LC lower cell

MAGIC Major Atmospheric Gamma Imaging Cherenkov

PE photoelectron

PMT photomultiplier tube

RMS Root Mean Square

SWGO Southern Wide-field Gamma-ray Observatory

UC upper cell

VERITAS Very Energetic Radiation Imaging Telescope Array System

WCD water Cherenkov detector

Acknowledgements

Finally, I would like to thank everyone who supported me during this thesis. In particular, I would like to thank:

- Prof. Dr. Christopher van Eldik for giving me the opportunity to work on this very exciting topic, the supervision of this thesis and his helpful comments in various meeting discussions.
- Prof. Dr. Stefan Funk for his helpful comments during the weekly meetings.
- Vikas Joshi for always being ready to listen to my questions and concerns and give good advice.
- my parents and my brother Max for their support during this thesis and throughout all my studies.

Statement of Authorship

I hereby declare that I have written this thesis without outside help and without using any sources other than those indicated. All thoughts or quotations which were inferred from these sources are clearly marked as such.

Erlangen, den 25.06.2021

Franziska Leitl